Biomedicine & Pharmacotherapy 198 (2026) 119304

Contents lists available at ScienceDirect

Biomedicine & Pharmacotherapy

journal homepage: www.elsevier.com/locate/biopha

A multivalent TAT–arginine-biodynamer conjugate targeting the bacterial cell envelope via specific membrane interactions

Mohamed A.M. Kamal [a,b,c], Walaa M. Metwally [a,b,c,d], Justine Bassil [a,b,c], Bart-Jan Niebuur [e], Tobias Kraus [e,f], Jennifer Herrmann [a,c,g], Marcus Koch [e], Anna K.H. Hirsch [a,b,c], Brigitta Loretz [a,c], Sangeun Lee [a,b,c,*], Claus-Michael Lehr [a,b,c,*]

[a] Helmholtz Institute for Pharmaceutical Research Saarland (HIPS), Helmholtz Centre for Infection Research (HZI), Saarland University, Saarbrücken 66123, Germany
[b] Saarland University, Department of Pharmacy, Saarbrücken 66123, Germany
[c] PharmaScienceHub, Saarland University, Campus A2 3, Saarbrücken 66123, Germany
[d] Alexandria University, Faculty of Pharmacy, Department of Pharmaceutics, Alexandria, Egypt
[e] Leibniz Institute for New Materials, Campus D2 2, Saarbrücken 66123, Germany
[f] Saarland University, Colloid and Interface Chemistry, Saarbrücken 66123, Germany
[g] German Center for Infection Research (DZIF), partner site Hannover - Braunschweig, Braunschweig 38124, Germany

ARTICLE INFO

Keywords:
Antimicrobial adjuvant
Gram-negative pathogens
Membrane permeabilization
Antibiotic potentiation
Synergy

ABSTRACT

Antimicrobial resistance is a global crisis driven by a scarce pipeline of new antibiotics. A major contributor is the intrinsic resistance conferred by the bacterial envelope, highlighting the need for innovative molecules for improved therapies. In this study, TAT–ArgBD, a conjugate of the cell-penetrating TAT peptide and arginine biodynamer (ArgBD), serves *in vitro* as a multivalent macromolecular antibiotic and synergist. TAT–ArgBD rapidly kills 99.9% of *Pseudomonas aeruginosa* at 32 μg/mL within 1 h, outperforming colistin, and shows minimum inhibitory concentrations (MICs) of 2–8 μg/mL against *Acinetobacter baumannii* and *Staphylococcus aureus*. Notably, it potentiates antibiotics such as novobiocin, chloramphenicol, and imipenem, leading to lowered MICs up to 256-fold. Notably, novobiocin, typically active only against Gram-positive bacteria, showed activity against Gram-negative bacteria when combined with TAT–ArgBD. Mechanistic studies suggest TAT–ArgBD antimicrobial and synergistic actions result from preferential binding to POPG and cardiolipin. This interaction induces bacterial membrane pore formation by adopting an α-helical conformation in the presence of bacterial lipids. With a favorable *in vitro* safety profile, a membranolytic index >64 and low mammalian cell toxicity at effective bactericidal concentrations, TAT–ArgBD's potential to enhance antibiotic efficacy, as well as function as a standalone treatment, supports further preclinical evaluation as an antimicrobial adjuvant.

1. Introduction

Antimicrobial resistance (AMR) has attracted increasing attention due to alarming projections over the coming decades, especially related to the emergence of multidrug-resistant (MDR) Enterobacterales, Carbapenem-resistant *Acinetobacter baumannii,* and Carbapenem-resistant *Pseudomonas aeruginosa* [1–3]. Several mechanisms contribute to the development of such MDR, but decreased antibiotic accumulation, either through reduced influx or increased efflux, is widely recognized as a universal resistance mechanism across various antibiotic classes [4]. Interestingly, membrane-acting antibiotics, such as polymyxins, do not have uptake into bacteria as a prerequisite for activity, but are a last resort in clinical guidelines due to resistance and safety concerns [5,6]. Another factor which makes addressing the MDR difficult is that most novel antibiotics are derivatives of existing antibiotic structures, with limited efforts directed at first-in-class antibacterial modalities. According to the World Health Organization (WHO), scarce antibiotic candidates with novel chemical structures are in clinical trials for systemic administration against Gram-negative bacteria, predominantly in phase I. Unfortunately, such candidates in a phase I clinical trial can have an expected success rate as low as just 7.9% [7,8]. Therefore, employing synergistic agents permeabilizing bacterial

* Corresponding authors at: Helmholtz Institute for Pharmaceutical Research Saarland (HIPS), Helmholtz Centre for Infection Research (HZI), Saarland University, Saarbrücken 66123, Germany.
E-mail addresses: sangeun.lee@uni-saarland.de (S. Lee), claus-michael.lehr@helmholtz-hips.de (C.-M. Lehr).

https://doi.org/10.1016/j.biopha.2026.119304
Received 8 November 2025; Received in revised form 14 March 2026; Accepted 27 March 2026
Available online 2 April 2026

membranes, like antimicrobial peptides or cell-penetrating peptides (CPPs), for poorly accumulating antibiotics, thereby achieving a synergistic effect against resistant bacteria, is raised as combination-therapy strategy.

HIV-1 TAT is a domain of the Tat viral protein and an established CPP that binds strongly to POPG, a major component of the bacterial lipid membranes. This interaction shows a K_d value of 7.5 μM (around 11 μg/mL) and as few as 4600 molecules to saturate the binding to one POPG liposome. Computational studies have suggested a mechanism for TAT translocation in which the cationic peptide first binds electrostatically to lipid phosphates, then induces lipid thinning and transient water pore formation that allow TAT to cross the bilayer. Because these pores are transient and collapse, free monomeric TAT is not expected to be antibacterial or cytotoxic [9,10]. In contrast to free CPP, multivalent polymer–CPP conjugates were prepared by conjugating CPPs like TAT onto a polymer backbone such as dextran. These conjugates form water channels simultaneously in addition to the backbone momentum. Conjugated TAT constructs (e.g., Nerinetide) have advanced to clinical trials supporting their potential applicability and safety for *in vivo* and human applications [11].

Polymer-peptide conjugates can lead to some damage to membranes, especially bacterial membranes, thereby synergistically enhancing the activity for poorly penetrating antibiotics. For example, WD40, enhanced clindamycin activity by up to 4096-fold [12–14]. Therefore, various types of polymers, both linear and branched, natural and synthetic, have been explored as backbones for polymer–CPP conjugates [15–17]. In this context, dynamic polymers may allow for flexibility and freedom to interact with the bacterial membrane, compared to rigid polymers as a backbone. Arginine–biodynamer (ArgBD) was recently studied for its dynamicity, biocompatibility, and physicochemical properties in literature, which make it suitable for biological applications [18–21]. Furthermore, in a previous study, we proved that ArgBD alone significantly potentiated the efficacy of colistin against Gram-negative strains. ArgBD targets the LPS of Gram-negative bacteria and changes their secondary structure in the LPS microenvironment, especially at the interface with the lipid A component. The structural changes allowed for better accessibility into the bacterial cell envelope and could potentiate the effect of antibiotics, including colistin [22].

In this study, we introduce a TAT–ArgBD conjugate to target both the LPS, and membrane lipids via ArgBD and HIV-1 TAT, respectively. This could enable bacterial selectivity via concurrent interactions with LPS and anionic phospholipids because bacteria uniquely present LPS together with anionic membrane lipids in the cell envelope. By conjugating TAT and ArgBD, we anticipated an enhanced engagement of bacterial envelopes through TAT's rapid membrane interaction from multivalency, along with the potentiating effect derived from ArgBD, as shown in Fig. 1. Therefore, we compared the antibacterial effects of TAT–ArgBD, as well as its synergistic effects with conventional antibiotics on several bacterial strains.

2. Materials and methods

2.1. Materials

L929 (ATCC-CCL-1) cells were obtained from LGC Standards (Molsheim, France). RAW264.7 cell line was obtained from ECACC (Salisbury, UK). *Staphylococcus aureus* Newman was provided by Prof. Marcus Bischoff from Saarland University hospital. *Escherichia coli* MG1655 (DSM18039), *A. baumannii* (DSM-30008), *P. aeruginosa* PA01 (DSMZ 22644), and *P. aeruginosa* PA14 (DSMZ 19882) were obtained from DSMZ (Braunschweig, Germany). RPMI 1640 medium, FCS, and Trypsin-EDTA were obtained from Thermo Fisher Scientific (Waltham, USA). PrestoBlue™ Cell Viability Reagent was obtained from Sigma-Aldrich (St. Louis, USA). Lactate Dehydrogenase (LDH) Cytotoxicity Detection Kit (11644793001) was obtained from Roche (Penzberg, Germany). Mueller Hinton broth (MHB) was obtained from Scharlau microbiology (Barcelona, Spain). M9 Minimal salts 5x Powder was obtained from SERVA (Heidelberg, Germany). TritonX-100 (CAS: 9036–19–5) was obtained from Sigma-Aldrich (St. Louis, USA). Free TAT peptide HpG(Homopropargylglycine)-GRKKRRQRRR was ordered from Genscript (Rijswijk, Netherlands). Paraformaldehyde methanol-free solution (16%) was obtained from Thermo Fisher Scientific (Waltham, USA). Glutaraldehyde 25% in H_2O was obtained from Sigma-Aldrich (St. Louis, USA). Hexamethyldisilazane (CAS: 999–97–3) was obtained from Sigma-Aldrich (St. Louis, USA) Novobiocin (CAS: 1476–53–5), Imipenem monohydrate (CAS: 74431–23–5), Chloramphenicol (CAS: 56–75–7), Colistimethate Sodium (CAS: 8068–28–8), Colistin Sulphate (CAS: 1264–72–8), Ciprofloxacin (CAS: 86393–32–0), Meropenem (CAS: 119478–56–7), Ceftazidime (CAS: 78439–06–2) were obtained from Cayman Chemical (Michigan, USA), Molekula Group (München, Germany), Sigma-Aldrich (St. Louis, USA), Cayman Chemical (Michigan, USA), AdipoGen Life Sciences (Fuellinsdorf, Switzerland), TCI chemicals (Eschborn, Germany), Sigma-Aldrich (St. Louis, USA), LKT Labs (Minnesota, USA) respectively. Lipopolysaccharides from *E. coli* O111:B4 (L4391) was obtained from Sigma-Aldrich (St. Louis, USA), 1,1′,2,2′-tetra-(9Z-octadecenoyl) cardiolipin (sodium salt) Cardiolipin, 1-hexadecanoyl-2-(9Z-octadecenoyl)-sn-glycero-3-phosphoethanolamine (POPE), 1-hexadecanoyl-2-(9Z-octadecenoyl)-sn-glycero-3-phospho-(1′-rac-glycerol), sodium salt (POPG) were obtained from Avanti Polar Lipids Inc. (Alabaster, AL, USA), Calcein (MW 622.53) was purchased from Sigma-Aldrich. (Saint Louis, Missouri, USA), Oxoid™ Sheep blood (SR0051B) was obtained from Thermo Fisher Scientific (Waltham, USA).

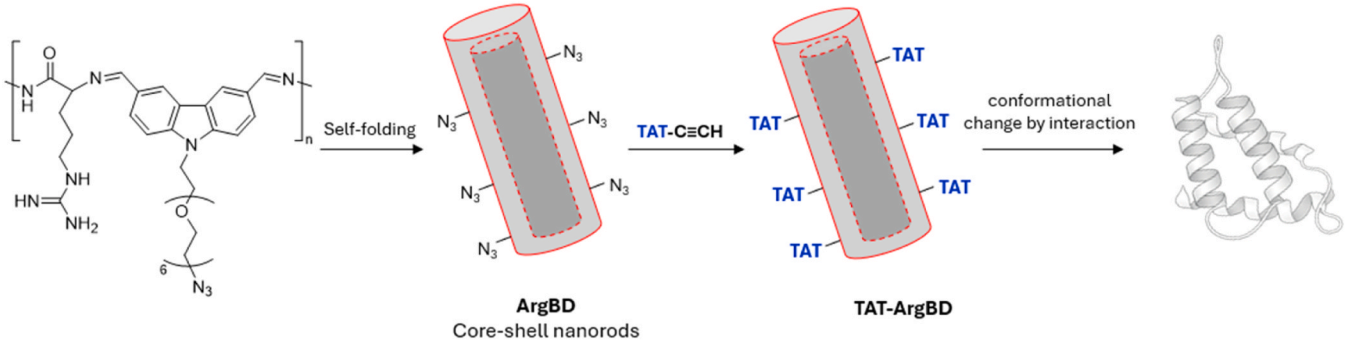

Fig. 1. Scheme illustrating ArgBD folding, followed by conformational modulation induced by membrane interaction. ArgBD is initially formed under acidic conditions via dynamic covalent chemistry, forming the ArgBD backbone. Subsequent constitutional dynamic chemistry drives self-folding of the polymer into an ordered core–shell nanostructure, where the core is composed of CA and the shell consists of HEG, stabilized by hydrophobic interactions and π–π stacking. TAT is conjugated onto the nanorod surface via Cu-assisted click chemistry (CuAAC), followed by conformational change upon interaction with the target.

2.2. Peptide quantification and conjugation rate calculation

Quantification followed standard qNMR principles using an internal standard [23]. To quantify the TAT content/purity, free TAT or TAT–ArgBD were dissolved in Deuterium oxide with maleic acid as an internal standard, then 1H-NMR was measured on a Bruker AV500 (500 MHz) spectrometer. The following equation was applied to calculate the concentration of the TAT:

$$P_{sample} = \frac{I_{sample} * N_{Ref} * M_{sample} * C_{Ref} * P_{Ref}}{I_{Ref} * N_{sample} * M_{Ref} * C_{sample}}$$

Where P, I, N, M, C stand for purity, integral, number of protons, molecular weight, and w/v concentration. The purity of the maleic acid and the TAT was assumed to be 100% as the purity of the maleic acid ≥ 99% and TAT–ArgBD was later washed to eliminate any unreacted impurities. The maleic acid proton signal at ppm 6.3 was used as the reference, while a methylene signal on the lysine residue at ppm 2.8 was used as the sample signal. The measured concentrations of TAT in the free TAT sample and TAT–ArgBD were then adapted in all of the following experiments to ensure that no bias would arise due to different quantification methods.

To calculate the conjugation rate, two methods were applied. First, TAT–ArgBD, which has X mg worth of TAT content (quantified via qNMR), was measured on a sensitive balance (referred to as gravimetry method). The following equation was then applied to determine the conjugation rate:

$$Conjugation\ rate\left(\frac{mol}{mol}\right) = 100\% * \frac{Mass(X)_{TAT} * Mwt_{TAT-ArgBD\ repeating\ unit}}{Mwt_{TAT} * Weighed\ Mass_{TAT-ArgBD}}$$

The measurement was repeated twice using two batches and standard deviation was calculated accordingly.

As a secondary method (referred to as qNMR method), the ratio of the integrations of the methylene on Arginine (ppm 3.1) and Lysine (ppm 2.8) as the ArgBD backbone has indeed one arginine residue. The following equation was employed to determine the conjugation rate:

$$Conjugation\ rate\left(\frac{mol}{mol}\right) = 100\% * \frac{I_{Arg\ in\ TAT-ArgBD} - I_{Arg\ in\ ArgBD}}{I_{Arg\ in\ TAT}}$$

Where I is the integral. The integral of Lysine methylene was assumed to be equal to 4.0 in the software; hence, the integral of the arginine could be calculated. The $I_{Arg\ in\ ArgBD}$ was assumed to be 2.0 as every repeating unit in the backbone can only have exactly one arginine residue (not more, not less). This procedure was performed twice for different batches using the TopSpin 4.4; hence, the standard deviation could be calculated.

Conjugation rate using absorbance was calculated as well, where the assay was developed by the authors for the purpose of this study. The quantification of ArgBD and TAT was based on four principles:

1. The quantification had to be based on a wavelength away from the newly formed aromatic triazole absorbance and closer to the amide bond absorbance (200 nm) to avoid interference.
2. The signal to background ratios of TAT–ArgBD, TAT, and ArgBD were high and most acceptable in each of them at 216 nm, so this wavelength was selected for the analysis
3. Since TAT–ArgBD was washed extensively, the signal at 216 nm is supposed to come from ArgBD and TAT, so the following equations were concluded:

$$Absorbance\ at\ 216\ nm_{TAT-ArgBD} = a * Absorbance\ at\ 216\ nm_{TAT} + b * Absorbance\ at\ 216_{ArgBD} \quad (1)$$

$$a + b = 100\% \quad (2)$$

Where a and b variables are the % of the TAT and ArgBD in the TAT–ArgBD respectively.

4. Spectra of samples and blanks were measured using a quartz plates and 16 μg/mL were used which has Absorbance ≤ 1.5 to have linear quantification in the range 200–1000 nm

First, all spectra were normalized as the concentration of TAT–ArgBD was assumed to be unknown before this analysis by applying the following equation on every point of the spectrum:

$$Normalized\ absorbance_x = \frac{Absorbance_x - Blank\ Absorbance_x}{\sum (Absorbance_{200-1000\ \ nm} - Blank\ Absorbance_{200-1000\ \ nm})/n} \quad (3)$$

Where x is the wavelength at which the absorbance of the samples was considered

n is the number of wavelengths between 200–1000 nm, which is equal to 801.

The 216 nm normalized absorbance from Eq. (3) was then used with Eqs. (1) and (2) to solve for variables a and b. This procedure was done twice, and standard deviation was calculated.

To validate the conjugation calculation using absorbance, 17 μg/mL of ArgBD physically mixed with 32 μg/mL of TAT absorbance was measured and compared to 49 μg/mL mass concentration of TAT–ArgBD (32 μg/mL of TAT) and graphed to check if it is similar and to what degree.

Lipid-Conjugate dose-binding assay:

A fluorescence-quenching–based association assay was developed for this study, using standard quenching concepts [24]. Different molar lipid or LPS concentrations were diluted in a quartz plate in a 10 mM phosphate buffer at pH 7.4. Then an equal volume of 250 μg/mL of TAT–ArgBD was added to the wells to obtain different molar ratios. The fluorescence was measured after 2 h using the 301 nm excitation and 372 nm emission as well as 350 nm as excitation and 520 as emission. The fluorophores calibration was observed to be linear until 31.25 and 62.5 μg/mL, respectively. The lipids were weighed, dissolved in chloroform/methanol 3:1 solution, dried, suspended in 10 mM phosphate buffer, and sonicated for a few minutes. LPS (molecular weight was assumed to be 10 kDa) was directly suspended in 10 mM phosphate buffer and sonicated. 2 replicates were performed for each group. The binding was determined by the following equation:

$$\%Quenching = 100\% * \frac{Fl_{sample} - Fl_{lipid\ background}}{Fl_{TAT-ArgBD} - Fl_{Buffer}}$$

For all biological assays, the activity per TAT content in TAT–ArgBD was reported. IC_{50} is the concentration that inhibits fluorscence by 50%.

2.3. Conjugate time-kill against P. aeruginosa

Time-kill kinetics were assessed using CFU counting adapted from CLSI M26 standard. Different samples were diluted and prepared in M9 bacterial medium in a 96-well plate. An inoculum of around $5*10^{\hat{}}5$ CFU/mL as final concentration which was initially grown in Mueller Hinton

broth but diluted in M9 was added to the treatment. The plates were placed in an incubator at 37 °C while shaking on an orbital shaker at 160 rpm. At the specific time point, samples were taken and serially diluted up to 10^8 in sterile PBS. 3 spots (10 μL each) per dilution were pipetted on an LB agar plate and left to dry before placing in a 30 °C overnight for counting on the next day. After the colonies were counted, the original log CFU/mL concentration was calculated back. The detection limit was kept at 33 CFU/mL. 3 biological replicates, 2 technical replicates each (n = 6) were performed. The values were averaged, and the standard deviation was calculated.

2.4. Molecular weight determination via SLS

Molecular weight was estimated by static light scattering according to standard Rayleigh–Debye analysis using a Debye plot approach [25]. The samples were prepared in 10 mM phosphate buffer pH 7.4 in 1 cm light path cuvette, and then inserted into a Zetasizer ZS Series (Malvern Instruments Limited, Malvern, UK) equipped with a HeNE laser (JDS Uniphase) at wavelength of 633 nm. The dn/dc was assumed to be 0.185 mL/g as the conjugate consisted largely of peptide moieties and a refractive index of 1.33. The sample was measured multiple times with different concentrations to yield the Debye plot and the molecular weight estimate.

2.5. Size determination via DLS

Hydrodynamic size by DLS was measured following established practice for biomacromolecules and nanoparticles [26]. The sample was diluted in 10 mM phosphate buffer pH 7.4 at 1 mg/mL concentration in a 1 cm path length cuvette. The particle size of the sample was measured via dynamic light scattering using Zetasizer ZS Series (Malvern Instruments Limited, Malvern, UK) observed from 173° backlight scattering in triplicate.

2.6. Secondary structure of the conjugate in different microenvironments

The method was adapted from a previous publication with minor modifications [22]. 400 μL of 120 μg/mL worth of TAT were diluted in 10 mM phosphate buffer pH 7.4. POPE/POPG were mixed in 3:1 mol: mol ratio and prepared in the same manner as the dose-binding assay as mentioned above and finally diluted to 3.4 mM concentration. The samples were then loaded into 1 mm path length quartz cuvette and measured using a Jasco 1500 spectropolarimeter (Gross-Umstadt, Germany). The setting of the measurement was as follows: Temperature = 24 °C, Bandwidth= 1 nm, Number of accumulations = 16, Scanning speed = 20 nm/min. The measurements were smoothened according to the Savitzky-Golay algorithm [27].

2.7. Red blood cells (RBCs) hemolysis assay

The hemolysis workflow and calculation were performed as commonly described for membrane-active antimicrobials with some modifications due to the positive charges of the conjugate [28]. In two Protein Lobind® tubes, 100 μL of sheep whole blood was washed three times with 2 mL of PBS in a centrifuge at 1700 g for 2 min. The pellet was resuspended carefully in 11 mL of PBS. A dilution series, 50 μL each, of different samples was prepared in Lobind® tubes. The positive control was 5% TritonX. The tubes were put in a shaking heat plate at 60 rpm at 37 °C for 60 min. The tubes were centrifuged for 5 min at 1700 g and 20 μL were taken out carefully without touching the pellet, which was diluted with 50 μL of PBS in a flat-bottom 96-well plate. The amount of lysed RBCs was quantified via measuring absorbance at 414 nm. 2–3 replicates were performed for each group. The following equation was applied:

$$\%Hemolysis = 100\% * \frac{Abs_{(sample\ with\ RBCs)} - Abs_{(sample\ without\ RBCs)}}{Abs_{(TritonX\ with\ RBCs)} - Abs_{(PBS\ with\ RBCs)}}$$

2.8. Minimum inhibitory concentration in different strains

Due to the effects shown in Figure S1, Mueller–Hinton broth does interact with the TAT–ArgBD and quenches its fluorescence. This effect was previously described in literature for cationic macromolecules as the usual rich media, like Mueller Hinton broth, contain extracts from yeast or beef, which have so many undefined components which can bind to the macromolecules [29–33]. A bacterial growth medium with more and minimal defined components, hence, minimal bacterial media was used.

MIC testing was performed using the standard broth microdilution according to European Committee on Antimicrobial Susceptibility Testing (EUCAST) guidelines (ISO20776–1:2019) with some modifications and using a concentration range of 0.03–64 μg/mL for all treatments.

The test medium was changed to either M9 or RPMI 1640 supplemented with 20 mM glucose (RPMIGluc). For both media, a higher inoculum was used to support sufficient growth over the 24 h observation period in the modified culture medium. This was 5-fold higher than recommended by EUCAST. For M9, a final OD_{600} in the well of 0.0025 was used. While for RPMIGluc, initial cell concentration was adjusted to McFarland 0.5 and for testing, the cell suspension was further diluted 1:40 in RPMIGluc to support an inoculum of approximately 2.5 × 106 CFU/mL.

Tobramycin quality controls in the minimal media of *P. aeruginosa* PA14, *P. aeruginosa* PA01, *E. coli* MG1655, *E. coli* ATCC25922, *A. baumannii*, *S. aureus* Newman yielded MICs of 0.25, 0.25, 0.25, 0.125, 0.5–0.1, 8–16 μg/mL, respectively.

2.9. Synergy of TAT–ArgBD with antibiotics

Checkerboard synergy testing and FICI calculation were performed as described before with some modifications [34]. A dilution series (left to right) of the antibiotic was prepared in along all rows of the 96 well plate at 4x the target final concentration (25 μL). TAT–ArgBD dilution series was prepared in separate tubes at 4x the target final concentration and 25 μL was added to each of the column (top to bottom) to form a checkerboard plate. The inoculation and incubation were conducted as in the MIC assay.

Fractional inhibitory concentration index (FICI) was calculated using the following equation:

$$FICI = \frac{MIC_{TAT-ArgBD\ in\ combination}}{MIC_{TAT-ArgBD\ alone}} + \frac{MIC_{antibiotic\ in\ combination}}{MIC_{antibiotic\ alone}}$$

2.10. Conjugate interactions with different media

The intrinsic fluorescence readout and background subtraction strategy follows the same general approach used in our prior fluorescence-based binding. 450 μg/mL of TAT–ArgBD was diluted in 100 μL of different media. The solutions were left for 2 h to allow for interactions to take place. Fluorescence was measured using excitation 301 nm, emission 372 nm, and excitation 350 nm, emission 520 nm. 2 replicates were performed. The following calculation was performed to determine the signal coming from the TAT–ArgBD:

$$Signal = \quad Flu_{sample\ in\ medium} - Flu_{medium\ only}$$

2.11. Viability and cytotoxicity assay on mammalian cells

Cell metabolic activity was assessed using a resazurin-based assay and membrane damage via LDH release, following the kits manufacturer manuals. L929 (5000 cells/well) and RAW 264.7 (8000 cells/well) cells

were seeded in a 96-well plate in RPMI 1640 supplemented with 10% FCS and incubated until cells reached confluency with fresh medium change every second day. Cells were washed once with PBS, and then the samples were added to RPMI 1640 without FCS and incubated at 37 °C with 5% CO_2. Because protein corona formation can influence nanoantibiotic uptake and activity, a protein-poor medium was used [35]. Additionally, to avoid bias, the mammalian cells were also incubated in such medium because the antimicrobial (efficacy) assays were performed in minimal media or RPMI 1640 with glucose (protein poor) to have an unbiased selectivity index and comparison. Dead control was 2% TritonX and the live control was cells incubated in RPMI 1640. After 24 h, 50 μL of the cell supernatant was taken and put aside in another plate for the LDH assay. The cells were washed with PBS, then 10% PrestoBlue in PBS was added to the cells and incubated for a few hours, then fluorescence was measured at excitation of 535 nm and emission of 615 nm. 7–9 technical replicates (3 biological replicates) were performed. The following equation was applied to measure viability:

$$\%viability = 100\% * \frac{Flu_{treated\ cells} - Flu_{dead\ control}}{Flu_{live\ control} - Flu_{dead\ control}}$$

The LDH was performed according to the manual of the kit. Afterwards, the absorbance was measured at 492 nm. The following equation was applied to calculate the cytotoxicity:

$$\%cytotoxicity = 100\% * \frac{Abs_{treated\ cells} - Abs_{live\ control}}{Abs_{dead\ control} - Abs_{live\ control}}$$

For graphical clarity, we additionally marked conservative guide thresholds in the plots (80% metabolic activity for PrestoBlue® and 20% cytotoxicity for LDH release). The 80% threshold was selected as an early slightest metabolic impairment and is intentionally a little stricter than the ISO 10993–5 cytotoxicity criterion (<70% viability). The 20% LDH threshold is widely used as a practical cutoff indicating the slightest noticeable change under the microscope as established by our lab.

2.12. Bacteria morphological changes visualization

Fixation, graded dehydration, and HMDS drying were performed following established SEM biological-sample preparation workflows, with minor timing adjustments for bacterial samples [36]. Bacteria was grown until reaching the log phase in M9 medium (PA14) and RPMI with Glucose (*S. aureus*) then was treated for 2 h. Bacteria were then washed with PBS to remove the treatment and resuspended in PBS, which was fixed with 2% paraformaldehyde and 2% glutaraldehyde overnight. Bacteria were then dehydrated with increasing increments of ethanol 30%, 40%, 50%, 60%, 70%, 80%, 90%, 100% for 15 min each on silicon wafers in a well plate. Finally, Hexamethyldisilazane was added and removed after 15 min, then left overnight under a hood to dry. On the next day, the samples were gold-sputtered using Quorum Q150R ES sputter-coater (Gala Instruments GmbH, Germany). The samples were then imaged with Zeiss SEM EVO HD15 (Zeiss, Germany). The same findings were also verified in more than one overnight culture using another TAT-ArgBD batch.

2.13. Bacteriomimetic vesicles leakage assay

Liposomes containing calcein (60 mM) were prepared using thin-film hydration method as described above with minor modifications. A lipid mixture of POPG, POPE and MPEG-2000-DSPE at a weight ratio of 25:68:7 were dissolved in Chloroform/Methanol (3:1). The organic solvents were then evaporated using a rotary evaporator under reduced pressure (200 mbar) at 40 °C and 250 rpm, to obtain a thin lipid film. The produced film was subsequently hydrated with a calcein solution (60 mM) at pH 7.4. The hydration step was followed by sonication in water-bath sonicator at 40 °C for 60 min. Extrusion was then done through a 100 nm polycarbonate filter at 40 °C using Avnati™ Extruder set (Alabaster, AL, USA). Finally, free calcein was removed from calcein-encapsulated vesicles by ten successive washing steps using Centrisart® centrifugal filter devices with a 30 kDa molecular weight cutoff (MWCO) membrane (Sartorius AG, Göttingen, Germany) at 2000 × g and 4°C. The calcein-release experiments were initiated by mixing the suspension of calcein-encapsulated vesicles with PBS solutions of TAT-ArgBD, TAT, and ArgBD at concentrations ranging from 0.25 μg/mL to 16 μg/mL. PBS alone and 0.5% Triton X-100 were used as negative and positive controls, respectively. The change in fluorescence intensity due to calcein release from the vesicles was monitored with a Tecan Spark-Cyto Plate Reader (Tecan Trading AG, Switzerland). Excitation and emission wavelengths were set at 478 and 528 nm, respectively. 3 replicates were performed

The amount of calcein released was quantified using a calibration curve of free calcein and mixed with calcein-loaded vesicles suspension (to exactly simulate the samples). The positive control was quantified with a one-point calibration.

2.14. Morphology and particle structure of TAT–ArgBD

Vitrification by plunge-freezing into liquid ethane followed standard cryo-EM specimen preparation procedures [37]. A 3 μL droplet of 10 mg/mL TAT–ArgBD in 10 mM phosphate buffer was deposited on a holey carbon film (S147–4, Plano, Germany) and blotted to a thin liquid film for two seconds. The sample was then plunged into liquid ethane (T = 108 K) using Gatan (Pleasonton, USA) CP3 cryo-plunge system. The sample was afterwards transferred under liquid nitrogen to a cryo-TEM holder (Gatan 914) operating at T = 100 K. Finally, the sample was analyzed by a Cryogenic Transmission Electron Microscopy (cryo-TEM, JEM-2100 LaB6, JEOL, Akishima, Japan) at 200 kV and low-dose conditions.

2.15. Structural properties of TAT–ArgBD and TAT–ArgBD-treated vesicles

Vesicles were prepared in the same way as done in the circular dichroism (CD) section with minor modifications. First, the lipids used weight ratio was changed to 25:68:7 POPG:POPE:MPEG-2000-DSPE. Secondly, the vesicles were extruded at least 15 times through a 100 nm filter using Avanti™ Extruder set (Alabaster, AL, USA).

Small Angle X-ray Scattering (SAXS) measurements were performed on a Xeuss 2.0 instrument (Xenocs SAS, Grenoble, France). A collimated beam from the K_α-line of a copper X-ray source with a wavelength of λ = 1.54 Å was focused on the sample with a spot size of 0.25 mm^2. 2D scattering images were recorded using a Pilatus 300 K detector with pixel sizes of 0.172 × 0.172 mm^2 and a sample-to-detector distance of 1211 mm, calibrated using a silver behenate standard. The solutions were mounted into borosilicate capillaries and measured with an acquisition time of 600 s and azimuthally averaged to obtain $I(q)$. Here, q is defined as $q = 4\pi \times \sin(\theta/2)/\lambda$ with θ being the scattering angle. All measurements were repeated 5 times. As no signs of sample aging were observed, all scattering patterns of each sample were averaged. Scattering by the buffer was measured separately and subsequently subtracted from the data.

The Beaucage function was used to determine the radius of gyration, R_g, of TAT–ArgBD dissolved in buffer [38]. The scattering patterns of bacteriomimetic vesicles and bacteriomimetic vesicles treated with TAT–ArgBD was modelled using the scattering profile of a series of Gaussian electron density distributions, implemented in the X + software [39].

3. Results

3.1. TAT–ArgBD synthesis and characterization

We designed TAT–ArgBD by conjugating the TAT at the terminus of the hexaethylene glycol chain (HEG), a side chain of the ArgBDs, to

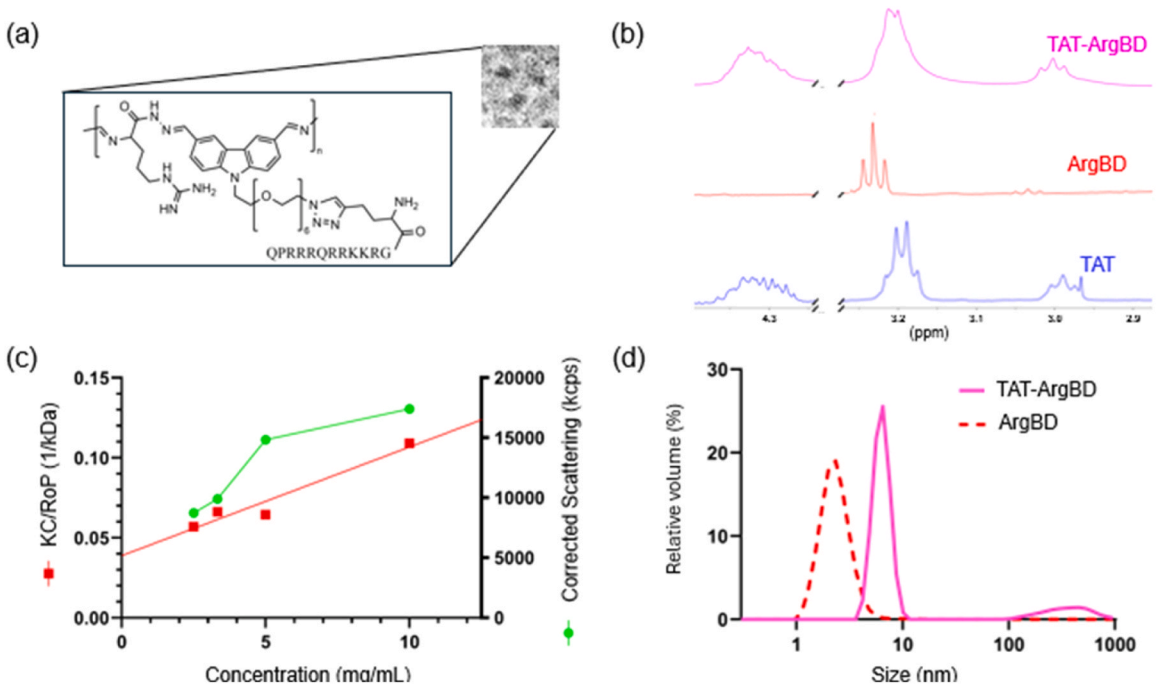

Fig. 2. (a) Cryo-TEM image of TAT-ArgBD and structure of TAT–ArgBD. (b) 1H-NMR spectra (ppm) showing (from left to right) peptide backbone, arginine δ methylene, lysine ε methylene after conjugating ArgBD to TAT. (c) Debye plot to determine the molecular weight by static light scattering (SLS) by measuring different concentrations of TAT–ArgBD yielding a molecular weight of 25.7 ± 4 kDa (KC/RoP y-intercept = 0.0389 ± 0.007 1/kDa, A2 second virial coefficient = 0.00339 ± 6.05e-4 mL·mol/g2, correlation coefficient (R2) = 0.94) (d) Volume particle size distribution as measured by dynamic light scattering (DLS) for TAT–ArgBD and ArgBD.

allow for flexibility of the peptide to interact (Fig. 2**a**). To conjugate TAT on the ArgBDs, we choose copper-catalyzed azide-alkyne cycloaddition (CuAAC) click chemistry, as it is known to be efficient for macromolecules. To achieve this, the monomer of ArgBD, HEG-conjugated carbazole dialdehyde (HEG-CA), was prepared based on previously reported methods [22] and further modified to introduce azide groups (-N_3). The N_3-HEG-CA was synthesized starting from 3,7-dibromocarbazole via lithium-halogen exchange and formylation with DMF, yielding CA. This compound was then alkylated with the commercially available N_3 chain and, after purification, afforded N_3-HEG-CA. Arginine hydrazide was synthesized by reacting *N*-methyl-D-arginine methyl ester with hydrazine hydrate in methanol for 24 h. The chemical structures of each compound were characterized using 1H-NMR and 13C-NMR spectroscopy, as detailed in the supplementary information (Figures S7-S13).

After synthesizing the monomers, we polymerized them, yielding ArgBD-N_3 by using Schiff-base reactions between aldehydes and primary amines. The polymerization was performed at a 1:1 mol ratio of N_3-HEG-CA with arginine hydrazide in the acidic aqueous solution for 24 h. Lastly, the alkyne-containing TAT was conjugated to the obtained ArgBD-N_3 using CuAAC to afford a triazole as a non-cleavable linker to get the structure shown in Fig. 2**a**. Details of the synthesis and 1H-NMR spectra are provided in the Supplementary Information.

The crude reaction mixture was washed extensively using centrifugal filtration (3 kDa MWCO) to remove salts, catalysts, and unreacted free TAT and monomers of ArgBD. Using 1H-NMR, UV-Vis absorption, and dynamic light scattering (DLS), we confirmed the presence of both TAT and ArgBD in the purified product. As seen in Fig. 2**b** and Figure S2, we observed clear TAT 1H-NMR peaks from the purified product, as well as typical UV-Vis absorption arising from carbazoles of ArgBD. We concluded the purified product includes both TAT and ArgBD with a molecular weight > 3 kDa, which evidences successful conjugation.

We then quantified the amount of TAT conjugated to ArgBD to determine the degree of TAT multivalency. Using quantitative NMR (qNMR), the conjugation rate was estimated to be 98 ± 0.64 mol/mol% or 67 ± 0.43 w/w% based on the arginine δ methylene and the lysine ε methylene 1H-NMR peaks shown in Fig. 2**b**. For comparison, gravimetric analysis yielded a conjugation rate of 102 ± 5.85 mol/mol% or 69 ± 4.0 w/w%. Lastly, based on UV absorbance, which was validated to have an accuracy of 96% (Figure S3), the conjugation rate was found to be 96 ± 0.22 mol/mol% or 65 ± 0.15 w/w%. All three measurements confirm a conjugation rate of roughly 98 mol/mol%, which is not unprecedented for CuAAC reaction.[25] [26], [27] The high conjugation rate suggests a robust platform for creating multivalent constructs.

The weight-average molecular weight of TAT–ArgBD was estimated using static light scattering (SLS) in aqueous buffer under native conditions. This solution-based method is well-suited for biodynamers because it avoids the distribution-bias and fragmentation that can arise for dynamic, polydisperse, reversibly linked conjugates. The dn/dc of protein was used as the TAT–ArgBD consists mainly of peptides (TAT) and the ArgBD is a peptide derivative composed of amino acids. SLS measurements indicated a molecular weight of 25.7 kDa, corresponding to around 12 repeating units of TAT–ArgBD per macromolecule, as shown in Fig. 2**c**. On the other side, it is known that ArgBD can spontaneously fold into a nanorod, so the conjugate could have a folded structure as well [18]. Thus, the hydrodynamic diameters (D_H) of the nanostructure formed by the conjugate (TAT–ArgBD) as well as the backbone (ArgBD) were compared. The volume-based D_H of TAT–ArgBD and ArgBD were 6.5 and 2.3 nm, respectively (Fig. 2**d**), which agrees with the cryo-TEM image at almost the resolution limit as shown in Figure S4 [18]. The radius of gyration (R_g) of the conjugate was measured to be 3.5 ± 0.2 nm using SAXS (Figure S5). The ratio between R_g (measured by SAXS) and hydrodynamic radius (R_h) (measured by DLS) provides insights into the macromolecular geometry of the conjugate and equals 1.1 in the case of TAT–ArgBD. This value is typical for soluble polymers with an extended chain conformation (a value of 0.77 is expected for a homogeneous sphere) [40]. Therefore, TAT–ArgBD is similarly expected to adopt an extended conformation.

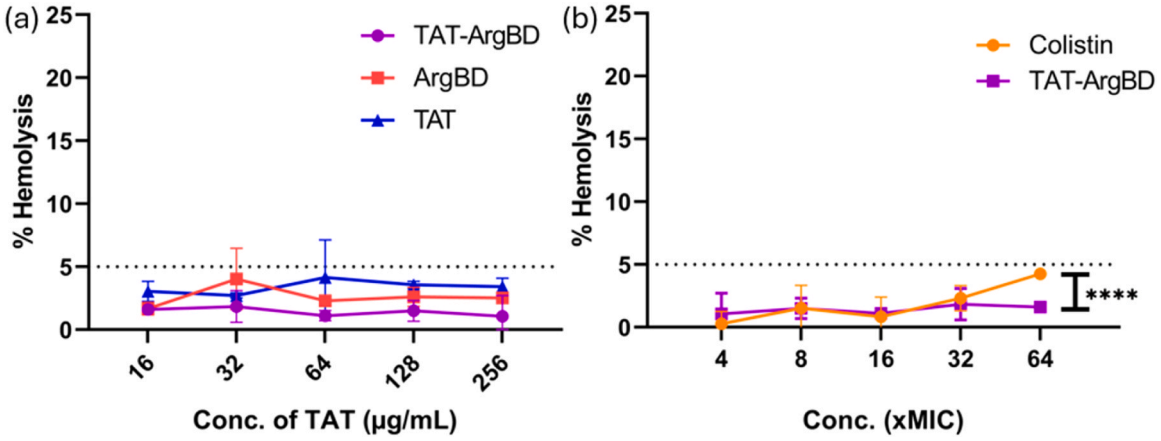

Fig. 3. RBCs hemolysis assay for (a) TAT–ArgBD and the forming moieties of the conjugate. For TAT–ArgBD and TAT, the concentration of TAT was shown on the x-axis was used, while for ArgBD sample the concentration of ArgBD backbone found in the conjugate at the respective concentration was used. In (b), the hemolysis assay comparison for TAT–ArgBD and Colistin at the same fold MIC assuming that TAT–ArgBD and Colistin MICs are 2 μg/mL and 0.5 μg/mL with significance test (for 64-fold MIC data point) via one-way ANOVA, **** represent p value of < 0.0001. 2–3 replicates were conducted.

3.2. Hemolysis and cytotoxicity towards mammalian cells

As a core safety parameter, the % RBCs hemolysis by TAT-ArgBD was conducted (Fig. 3). Multivalent peptide constructs often exhibit hemolytic activity. Yet, neither TAT–ArgBD nor its individual components induced significant hemolysis, even at concentrations well above the anticipated therapeutic levels (Fig. 3**a**). As for Fig. 3**b**, a head-to-head comparison of TAT–ArgBD and colistin was performed. At 64-fold MIC, TAT–ArgBD (256 μg/mL) was significantly superior to colistin (16 μg/mL) in terms of RBCs staying intact.

To assess the safety of the conjugate towards mammalian cells, L929 mouse fibroblasts were exposed at various concentrations for 24 h. 16 μg/mL of colistin and 256 μg/mL of TAT–ArgBD were chosen as the highest tested concentrations, which were later observed to be 64-fold MIC for both compounds. In terms of membrane damage (LDH release, Fig. 4**a–d** in black), TAT–ArgBD at concentrations $\leq$ 64 μg/mL ($\leq$16-fold MIC) showed no significant membrane damage toxicity (>20%). As shown in Fig. 4**e–h**, no reduced metabolic activity (PrestoBlue® assay) was observed except for $\geq$ 64 μg/mL of TAT–ArgBD [41, 42].

TAT–ArgBD cytotoxicity was further evaluated in RAW264.7 macrophages, representing immune cells, to ensure its safety across multiple cell types. In fibroblasts, TAT–ArgBD showed no significant cytotoxicity at any concentration tested (Fig. 3). Colistin induced mild membrane damage and reduced viability only at 16 μg/mL (Fig. 4**d,** 4**h**).

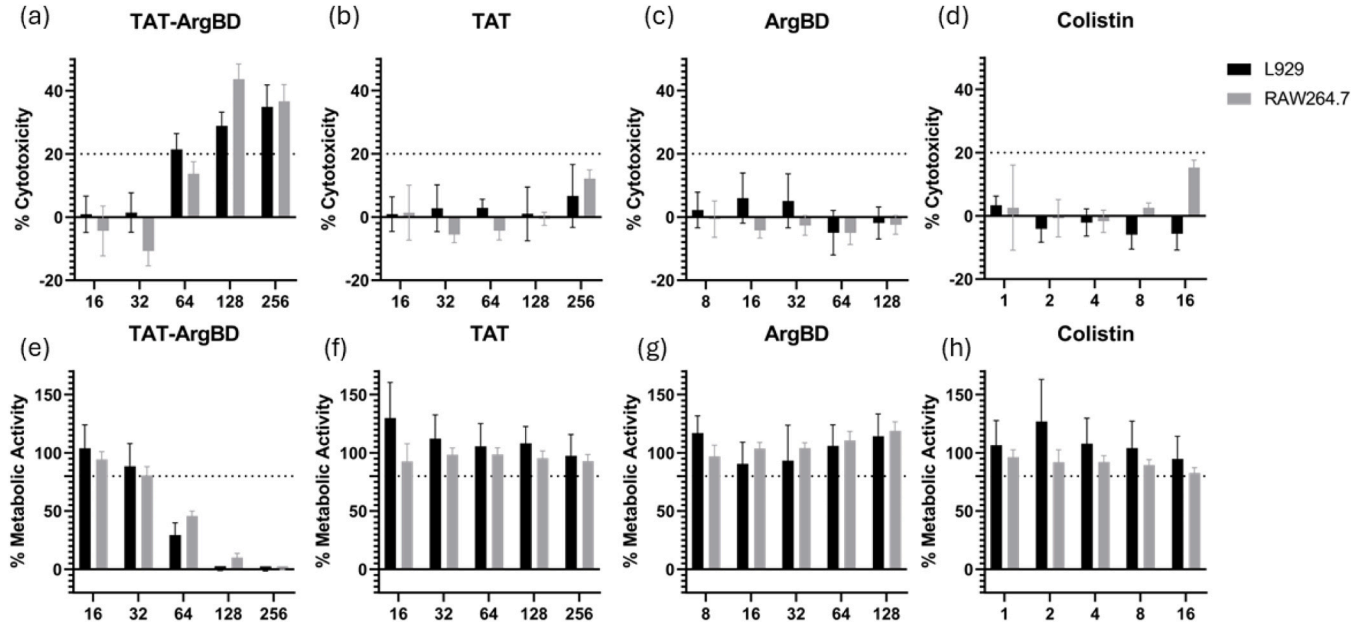

Fig. 4. Cytotoxicity assessment by using lactate dehydrogenase (LDH) assay with L929 fibroblasts (black) and RAW264.7 macrophages (grey) with (a) TAT–ArgBD conjugate, (b) free TAT peptide, (c) ArgBD, and (d) Colistin. Viability assessment using PrestoBlue® was used as well with L929 fibroblasts (black) and RAW264.7 macrophages (grey) to assess the metabolic activity in the presence of (e) TAT–ArgBD, (f) free TAT peptide, (g) ArgBD, and (h) Colistin. The dead control (assumed to be 100% cytotoxicity and 0% viability) was 2% TritonX in medium while the live control (assumed to be 0% cytotoxicity and 100% metabolic activity) was treated with just medium. The dotted line representing significant toxicity threshold was plotted at 20% cytotoxicity (LDH) and 80% viability (PrestoBlue®). For all subfigures, n = 7–9, N = 3. The mean was plotted, and error bars represent standard deviation.

Table 1
Minimum inhibitory concentration (MIC, μg/mL) of TAT–ArgBD, ArgBD, and TAT in different strains. n = 2–3.

	TAT–ArgBD	ArgBD	TAT
P. aeruginosa (PA14)	4	> 64	> 64
P. aeruginosa (PAO1)	4	> 64	> 64
E. coli MG1655	16	> 64	> 64
E. coli ATCC 25922	8	> 64	16
A. baumannii DSM 300008	2–8	> 64	> 64
S. aureus Newman	2	64–> 64	64–> 64

*Different media were used for different organisms as detailed in the methods section.

3.3. Antimicrobial activity

Having established the safety aspects for the TAT–ArgBD, its antimicrobial activity was investigated to evaluate its potential use as a stand-alone agent. The antimicrobial activity of ArgBD and TAT was also assessed to determine if they have any notable antimicrobial activity before they are conjugated. A MIC assay was conducted against a panel of Gram-negative (*P. aeruginosa, E. coli, A. baumannii*) and Gram-positive (*S. aureus*) strains. These well-characterized reference strains were deliberately chosen for this study. They serve as a reproducible proof-of-concept panel to benchmark the TAT–ArgBD platform across different species. In subsequent work, we aim to extend this analysis to clinical isolates of *P. aeruginosa* and *A. baumannii* to directly evaluate the performance of TAT–ArgBD combinations in clinically relevant resistance backgrounds. As shown in Table 1, the TAT–ArgBD showed good antimicrobial activity (MIC ≤ 4 μg/mL) against all strains except for *E. coli* (MG1655 and ATCC25922), while TAT and ArgBD, were generally not active. As an exception, TAT showed weak activity against *E. coli* ATCC 25922, which we cannot fully explain at this stage. However, it can be hypothesized that smooth *E. coli* (ATCC 25922) has a less protective/absorbent LPS than rough *E. coli* (MG1655), while *P. aeruginosa, A. baumannii,* and *S. aureus* are inherently different. It could also be noted that the multimeric nature caused TAT–ArgBD to have improved antimicrobial activity of ≥ 32 folds in *P. aeruginosa* compared to free TAT [14].

3.4. Mechanism of action

To elucidate the mechanism by which TAT–ArgBD exhibits antimicrobial activity, we investigated its interactions with the bacterial cell envelope using lipid-binding assay, SEM imaging, CD, and SAXS. We investigated the origin of the observed activity of TAT–ArgBD. Given that 1) TAT is known to target lipid bilayer [43], 2) TAT–ArgBD is a cationic macromolecule which might be targeting bacterial membranes [44,45] and 3) ArgBD has previously been shown to enhance antibiotic activity by interacting with LPS on the bacterial envelope [22], we hypothesized that TAT–ArgBD also exerts its antibacterial effects by targeting the bacterial envelope. Thus, we visualized the effect of TAT–ArgBD on the cell membrane using SEM. PA14 bacteria were incubated for 2 h with different concentrations (0, 4, 16 μg/mL) of TAT–ArgBD. PA14 bacteria clearly shows pores at an inhibitory, non-lethal concentration of TAT–ArgBD (4 μg/mL) hitting the bacterial cell envelope at a certain point causing the leakage of the intracellular components of the bacteria (Fig. 5**b**). Treatment with a higher likely lethal concentration of TAT–ArgBD (16 μg/mL) resulted in the formation of larger pores in the bacterial cell membrane, as depicted in Fig. 5**c**. This membrane disruption was accompanied by extensive damage, leading to bacteria cross-linking and the aggregation of cells into larger clumps. These observations support the hypothesis that TAT–ArgBD exerts its antibacterial effects through its action on the bacterial cell membrane. Similar results were also shown in *S. aureus*. At sublethal 2 μg/mL, *S. aureus* bacteria showed membrane damage as shown in Figure S6. This pattern of membrane damage is typically characteristic of membrane-active peptides targeting bacterial membrane and has been reported previously [46,47]. At higher lethal concentrations, only bacterial debris but no remaining bacteria could be observed.

Besides, the interaction of TAT–Arg with bacterial membranes was examined using model vesicles mimicking bacterial membranes composed of POPG, POPE, and cardiolipin. Fig. 6 shows the SAXS patterns of bacteriomimetic lipidic vesicles and bacteriomimetic lipidic vesicles treated with TAT–ArgBD. The SAXS pattern of the vesicles (Fig. 6**a**) shows forward scattering below $q = 0.02$ Å^{-1}, which is due to scattering by the entire vesicles and a broad peak centered around $q = 0.1$ Å^{-1}, resulting from scattering at the bilayers. A multilayer model with three Gaussian electron density profiles to describe the lipid headgroups in the inner layer, the methyl chains within the bilayers and the lipid headgroups in the outer layer, respectively, was used to model the scattering pattern. The data at small q-values (below 0.02 Å^{-1}) were excluded from the fit because the curvature of the bilayers as a result of the finite size of the vesicles was not included in the model. Fig. 6**b** presents the electron density profile of the bilayer in relation to distance from the bilayer center, z, resulting from the fit, normalized to that of the buffer. The distance between the maxima of the two outer peaks, representing the lipid head-groups in the inner and outer layer, which describes the thickness of the bilayer, and amounts to ~43 Å. The asymmetry of the profile is presumably due to density differences between the inner and outer parts of the bilayer, because of its curvature, like previously published SAXS measurements on vesicle systems, hinting towards a vesicle formation [48].

Similar to the SAXS pattern of vesicles, the TAT-ArgBD-treated bacteriomimetic vesicles (Fig. 6**c**) shows forward scattering below $q = 0.02$ Å^{-1}. However, the appearance of a double peak around $q = 0.1$ Å^{-1} indicates a strong change in the bilayer structure. A combination of four Gaussian electron density profiles is used to model the scattering curve. While the model reproduces the double peak, it should

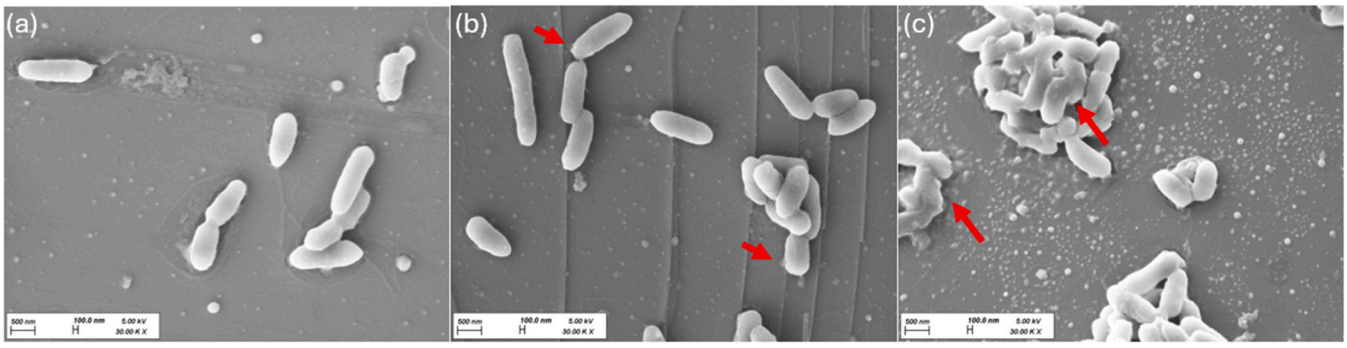

Fig. 5. Scanning Electron Microscopy of Pseudomonas aeruginosa PA14 bacteria after exposure for 2 h to different treatments, which are (a) no treatment, (b) 4 μg/mL of TAT–ArgBD, (c) 16 μg/mL of TAT–ArgBD. Red arrows point to intracellular components leaking from the membrane.

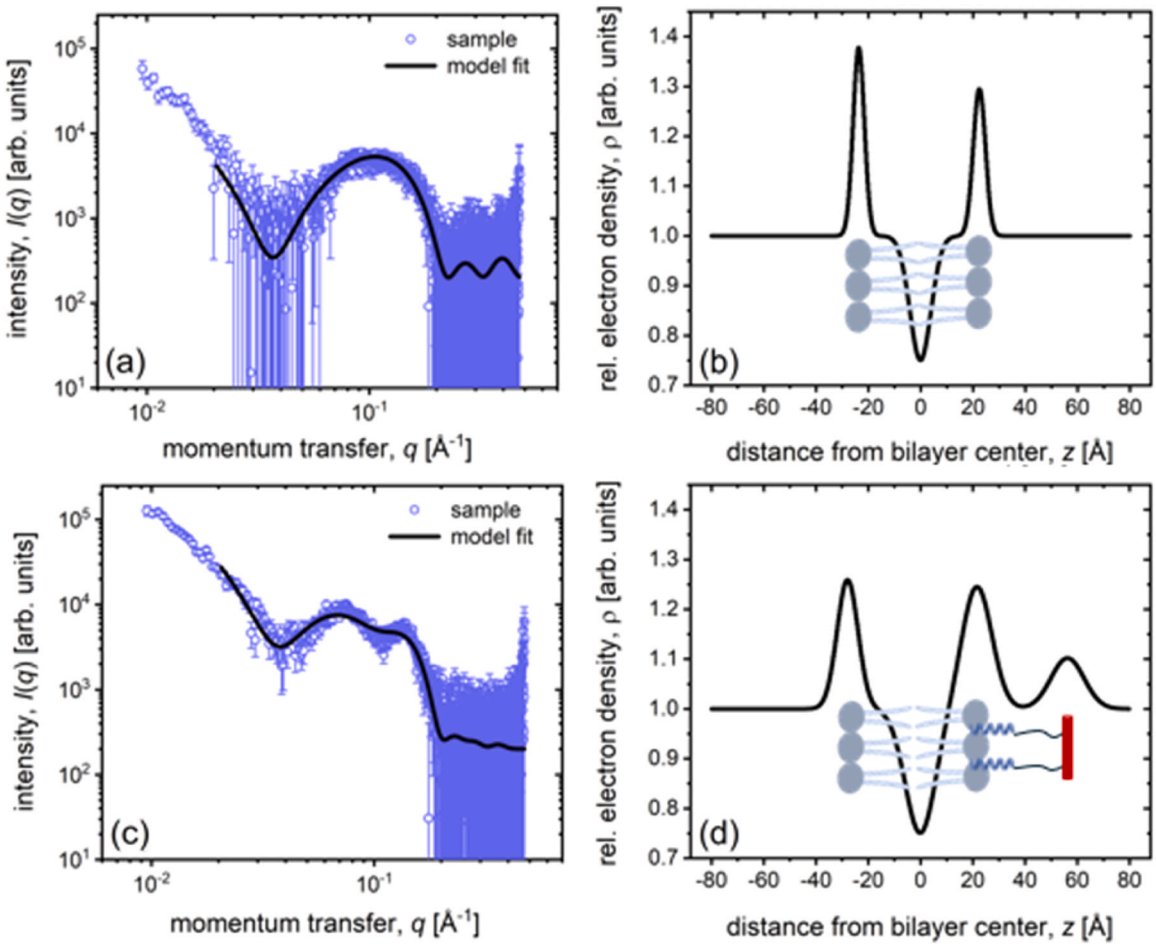

Fig. 6. Results from small angle X-ray scattering on bacteriomimetic lipidic vesicles and bacteriomimetic lipidic vesicles treated with TAT-ArgBD. (a) SAXS pattern of bacteriomimetic vesicles (blue data) and model fit using a multilayer model consisting of three Gaussian electron density profiles (black line). (b) The resulting electron density profiles without any treatment, in relation to distance from the bilayer center, z, with sketched lipids forming a lipid bilayer (c) SAXS pattern of bacteriomimetic vesicles treated with TAT-ArgBD (blue data) and model fit using a multilayer model consisting of four Gaussian electron density profiles (black line). (d)The resulting electron density profiles of vesicles treated with TAT-ArgBD in dependence on distance from the bilayer center, z, with sketched conjugate with varying position partially embedding into the lipid bilayer.

be noted that there are slight differences between the shape of the peaks of the SAXS pattern and those predicted by the model. Therefore, only a qualitative description of the results is possible. The resulting electron density profile, shown in Fig. 6**d**, gives insights into the bilayer structure, and shows an average bilayer thickness to ~43 Å. Several observations can be made. Firstly, a broadening of the Gaussians describing the lipid headgroups (around z = -25 Å and z = 25 Å, respectively) and methyl chains in the interior of the bilayers (at z = 0) indicates a more heterogeneous structure as compared to bacteriomimetic vesicles in the absence of TAT–ArgBD. Secondly, the enhanced electron density around z = 60 Å indicates that the center of mass of the conjugate is located very close to the bilayers-solvent interface outside the bilayer, representing the normal distribution of conjugates closer to and further from the center of the layer. Both observations hint towards the embedding of the conjugate into the outer part of the bilayer, leading to the effects seen *in bacterio*, as elaborated by the sketch in Fig. 6**d**. This hypothesis is furthermore supported by the increased symmetry of the Gaussians describing the lipid headgroups: The presence of the conjugate increases the electron density on the outer part of the vesicle, reversing the lowered density due to the curvature of the vesicles to become almost equal, hinting towards deterioration of the vesicular structures.

To further understand the mechanism, we studied how TAT–ArgBD interacts with lipids by analyzing its intrinsic fluorescence properties. A strong interaction was hypothesized to result in fluorescence quenching as TAT–ArgBD binds to lipid vesicles. We plotted this quenching effect against the molar ratio of TAT–ArgBD to the lipids POPE, cardiolipin, and POPG (Fig. 7). These lipids were selected as key representatives of bacterial membranes, given that the bacterial cell envelope is largely composed of phospholipids, namely POPE, cardiolipin, and POPG, which are particularly abundant and play critical roles in maintaining the structure and function of Gram-negative and Gram-positive bacterial membranes, making them an appropriate focus for this study [49].

As for the anionic POPG, the IC_{50} values of the fluorescence quenching with POPG could be calculated as 0.287 mol/mol ± 0.013 (emission at 372 nm) and 0.267 mol/mol ± 0.016 (emission at 520 nm) (Fig. 7**a**). Meanwhile, for cardiolipin, the values were also similar, specifically, the IC_{50} values were 0.267 mol/mol ± 0.003 (emission at 372 nm) and 0.25 mol/mol ± 0.019 (emission at 520 nm) (Fig. 7**b**). The zwitterionic POPE was tested with no observed binding with TAT–ArgBD up to the highest tested ratio (Fig. 7**c**). While the binding with the LPS could not be assessed, as LPS could not be solubilized at the molar ratio due to its very high molecular weight. This agrees with the fact that both interacted lipids are anions and close in chemical structure, hence can attract cationic molecules [39]. To visualize this interaction on a molecular level, it can be estimated that one TAT moiety binds approximately four lipid molecules at the IC_{50}. While this estimation does not allow for definitive conclusions, it suggests that the activity does not follow a conventional 1:1 binding modality, as seen in

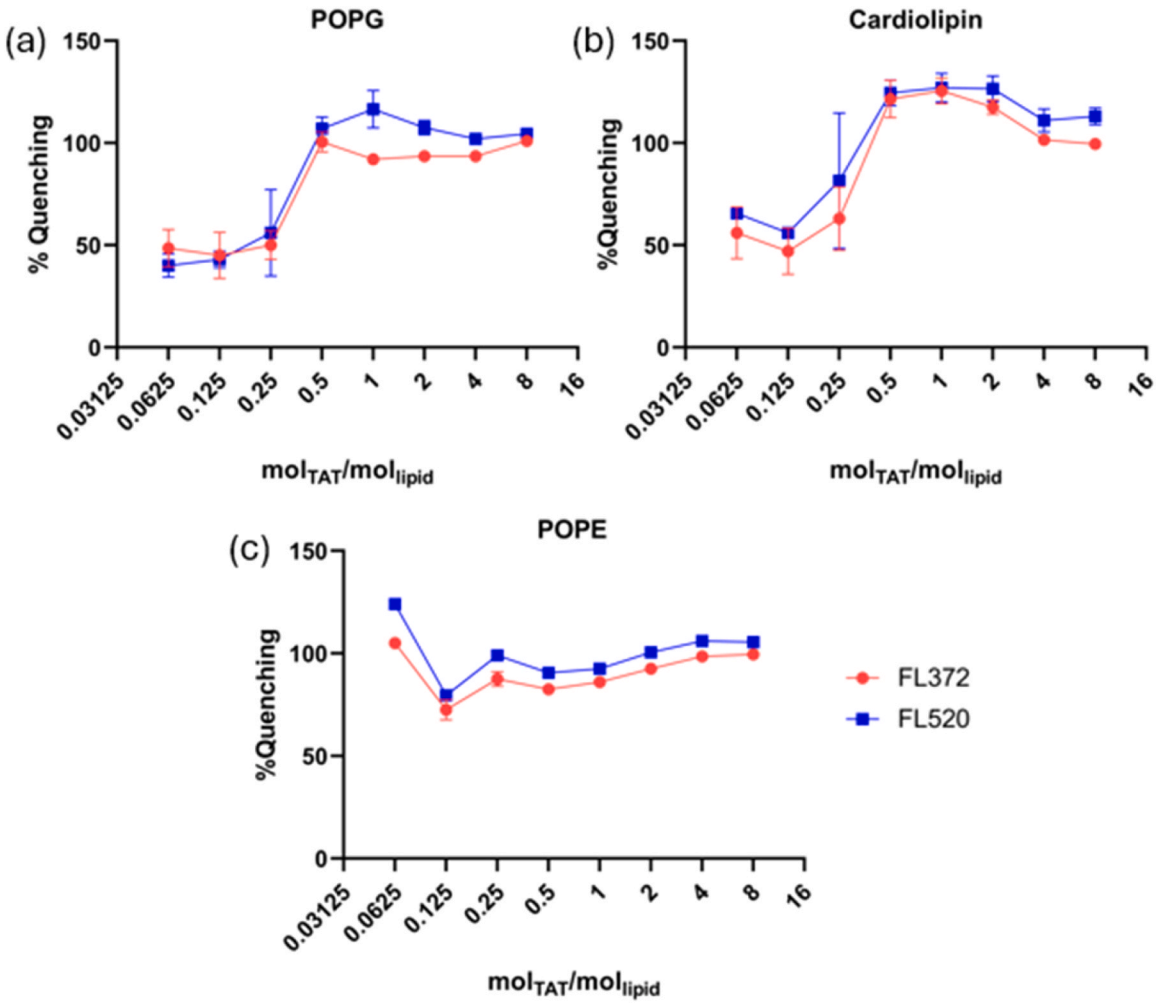

Fig. 7. Dose-response curve of fluorescence quenching of TAT–ArgBD following two fluorophores (excitation 301 nm, and 350 nm with emission of 372 nm, and 520 nm, respectively) with (a) POPG, (b) Cardiolipin, and (c) POPE.

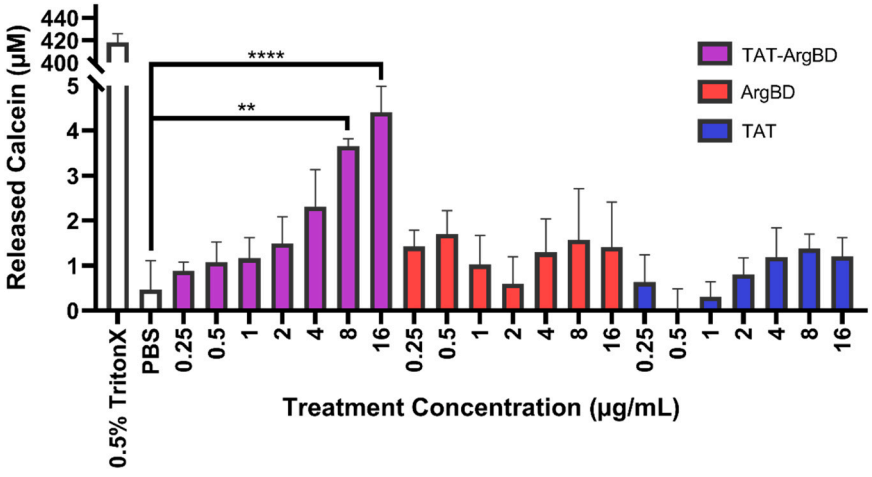

Fig. 8. Calcein leakage assay where different concentrations of treatments (TAT-ArgBD, ArgBD, TAT) were applied to the vesicles for 50 min. Released calcein is quantified for every group and reflects the degree of the vesicles' disruption. PBS was used a negative control, while 0.5% TritonX was used as a positive control (releases all calcein). One-way ANOVA significance was utilized to compare PBS Control with the TAT-ArgBD, ArgBD, TAT treatments. ** indicates $P \leq 0.01$, **** indicates $P \leq 0.0001$ compared to PBS, otherwise no significance exists.

enzyme-substrate interactions. Instead, it points toward a more complex mechanism, likely influenced by the conformation of the lipid-TAT–ArgBD complex within bacterial membranes.

To assess pore formation and its dependence on bacterial lipids, a calcein vesicle leakage assay was used. Calcein is a self-quenching dye with minimal fluorescence at very high concentration and enhanced fluorescence in lower concentrations [50]. Bacteriomimetic lipid vesicles without LPS were loaded with highly concentrated calcein, and the membrane permeabilization was quantified by measuring fluorescence increase following treatment with ArgBD, TAT, and TAT–ArgBD. As shown in Fig. 8, ArgBD and TAT showed no significant difference compared to negative control (PBS). Also, no non-significant dose-dependent effect was observed as well. TAT-ArgBD (8 and 16 μg/mL) showed significant increase in the calcein response compared to PBS control. Additionally, TAT–ArgBD showed a clear dose-dependent trend indicating a clear vesicle disruption only by TAT–ArgBD.

To investigate the secondary structure of TAT–ArgBD depending on the peptide bond polarization of light, CD measurements were performed. Due to the presence of ArgBD aromatic system in combination with the high lipid concentration, the absorbance led to increase in the dynode voltage. Therefore, only wavelengths above 200 nm were considered for the secondary structures analysis. In buffer and the absence of any lipids, TAT–ArgBD exhibited a predominant random coil structure, characterized by a negative peak near 200 nm. A very slight triple helix character was observed, with a $-\theta_{200}/\theta_{220}$ ratio of 16.23, which is substantially lower than that for collagen for instance (Fig. 9**a**). [51] In the presence of SDS, which mimics vesicular structures, no difference was noted from the in-buffer spectrum (Fig. 9**b**). Similarly, in a hydrophobic lipid mimicking environment (50% Trifluoroethanol), no significant differences were noted (Fig. 9**c**). This indicates that TAT–ArgBD has no tendency for a certain secondary structure in lipid membranes in general. With the vesicles made of a mixture of POPE and POPG, TAT–ArgBD displayed a pronounced α-helical structure, evidenced by distinct negative bands near 208 nm and 222 nm (Fig. 9**d**). These findings demonstrate that TAT–ArgBD does not adopt an organized secondary structure in buffer, lipid-like, or hydrophobic environments. However, its significant transition to an α-helical conformation in the presence of POPE/POPG vesicles suggests selective targeting of bacterial membranes [52,53].

3.5. Bacteria killing kinetics

Having established that TAT–ArgBD interacts with the bacterial cell envelope, we next evaluated the antimicrobial efficacy over time. A time-kill assay was conducted using CFU counting to determine the speed and extent of bacterial clearance.

We performed time-kill kinetics only in *Pseudomonas aeruginosa* (PA14). This strain was selected because *P. aeruginosa* is a clinically relevant, hard-to-treat Gram-negative pathogen frequently associated with hospital-acquired infections and multidrug resistance. In this study, PA14 also served as our lead Gram-negative model for benchmarking both the stand-alone bactericidal activity of TAT–ArgBD and its antibiotic-potentiating effects; notably, the strongest and most clinically informative synergy signals were observed in PA14. Because CFU-based time-kill assays are labor-intensive and require dense sampling, we prioritized this strain to quantify killing rate and extent.

As shown in Fig. 10**a**, 8 μg/mL of TAT–ArgBD caused a 1-log decrease of PA14 bacteria within an hour, while higher doses (32 μg/mL) achieved even 3-log (99.9%) bacterial killing within the same time period. The maximum killing occurred within the first hour and the curve approached a plateau after ~6 h (for both TAT-ArgBD and colistin). Such plateaus in time-kill experiments can reflect reduced effective exposure over time (e.g., compound degradation/instability during incubation or sequestration/adsorption to biomass and surfaces) and/or survival of a tolerant subpopulation. These possibilities were not distinguished in the present study.

In Fig. 10**b**, TAT–ArgBD was compared with its individual chemical components (ArgBD and TAT) without covalent bonding. Neither the individual components nore their physical mixture showed any activity against PA 14. However, a mild growth inhibition was noticed in the case of free TAT, hence, TAT is considered here as the active moiety of the TAT–ArgBD conjugate. The concentrations of TAT and ArgBD were calculated based on the conjugation rates, corresponding to their respective masses in 32 μg/mL conjugated TAT in TAT–ArgBD.

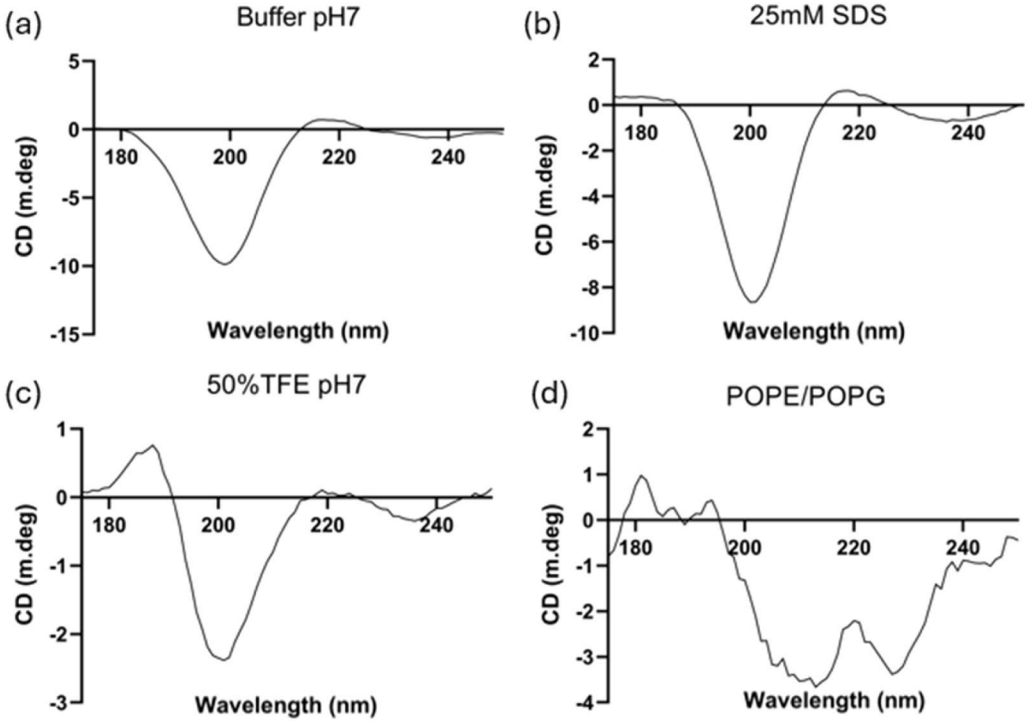

Fig. 9. Circular dichroism (CD) spectra of TAT–ArgBD in (a) phosphate buffer, (b) SDS, (c) 50% TFE, (d) POPE/POPG vesicles.

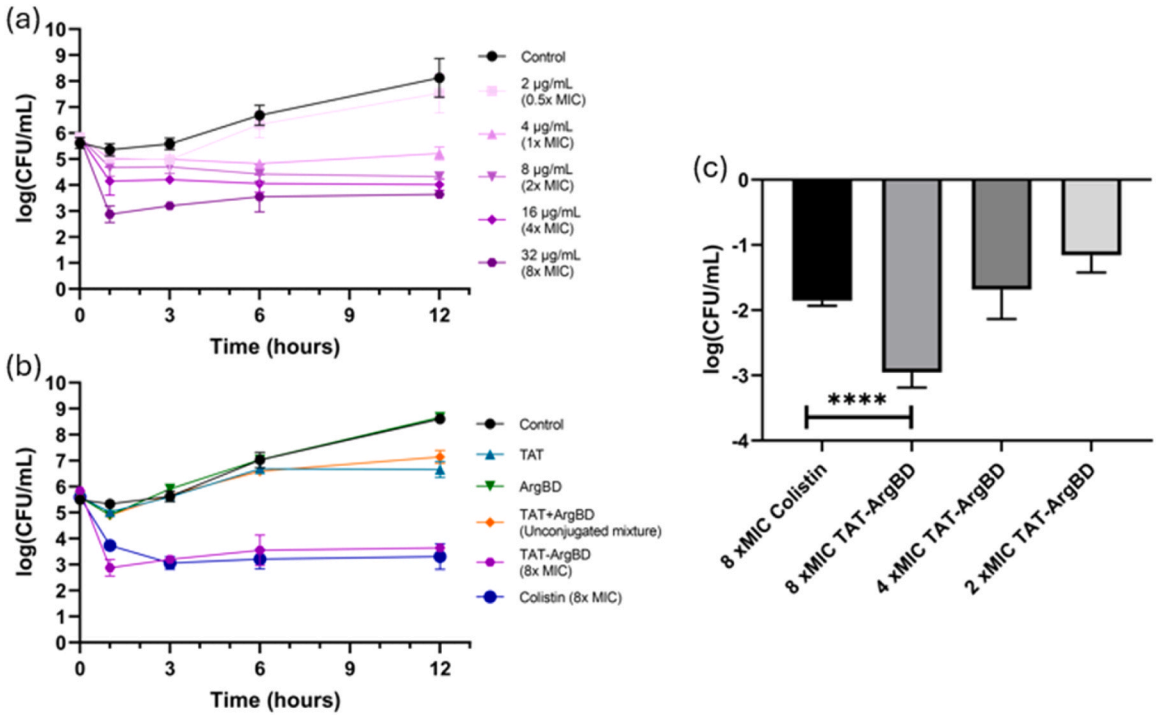

Fig. 10. Time-kill assay for Pseudomonas aeruginosa PA14 for (a) different concentrations of TAT–ArgBD in the range of (0.5–8 -fold MIC), and (b) 32 μg/mL of TAT–ArgBD (8-fold MIC) conjugates compared to its single chemical components (32 μg/mL TAT and 16 μg/mL ArgBD) having the equivalent amount and their unconjugated physical mixture as well as comparison with 2 μg/mL of Colistin (8-fold MIC). (c) Head-to-head comparison of the decrease of the PA14 count after just 1 h of treatment. **** represents $p < 0.0001$ on one-way ANOVA.

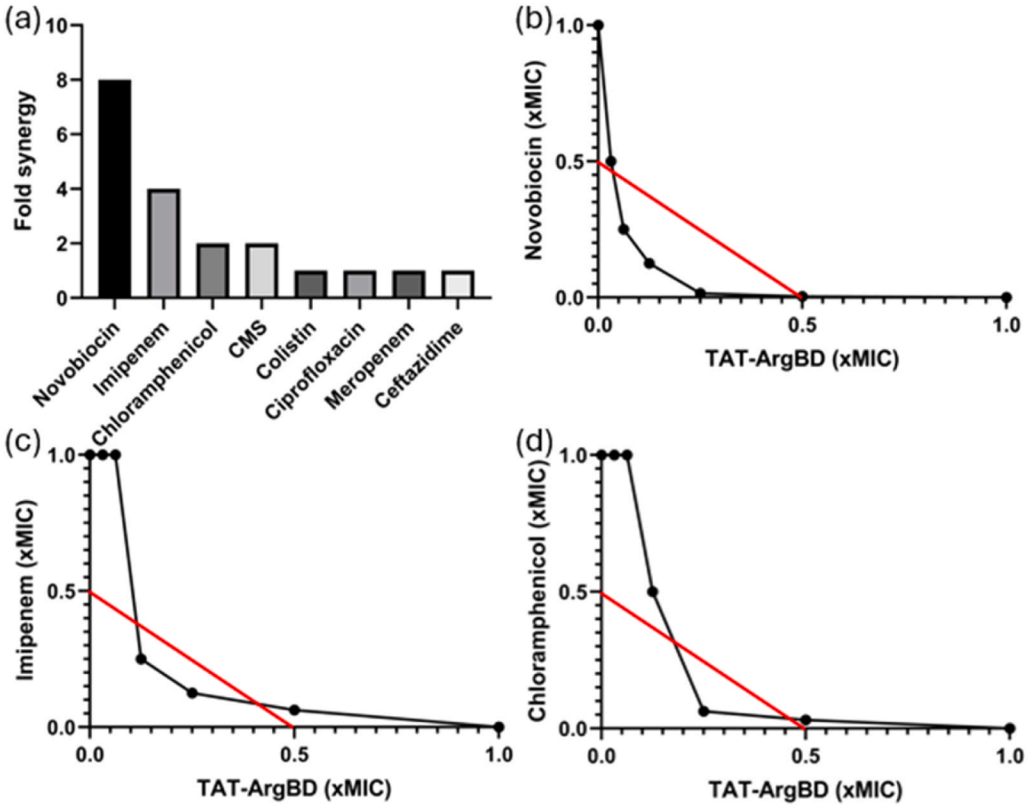

Fig. 11. (a) Synergy in Pseudomonas aeruginosa PA 14 depicted by fold MIC reduction when various antibiotics are combined with 0.5 μg/mL (0.125-fold MIC) of TAT–ArgBD. Checkerboard assays for TAT–ArgBD in combination with (b) Novobiocin, (c) Imipenem, and (d) Chloramphenicol. Lower left of the red line represents FICI of ≤ 0.5 (significant synergy). MICs of TAT–ArgBD, Novobiocin, Imipenem, Chloramphenicol, Colistimethate Sodium (CMS), Colisitn, Ciprofloxacin, Meropenem, Ceftazidime were 4, 256, 0.5, 32, 0.5, 0.25, 0.25, 0.125, 2 μg/mL.

Additionally, 2 μg/mL of colistin (8-fold MIC) was compared to 32 μg/mL of TAT–ArgBD (8-fold MIC) in terms of the killing kinetics, as colistin is an established antibiotic with a membrane-targeting mechanism of action [37]. As a result, 8x MIC TAT–ArgBD showed 99.9% killing efficiency versus 98.6% for 8x MIC colistin within the first hour against PA14. (Fig. 10**b and** 10**c**). However, the killing kinetics of TAT–ArgBD and colistin were comparable after 3 h. TAT–ArgBD demonstrated a concentration-dependent rapid elimination of PA14 bacteria within minutes of exposure. Its superior killing kinetics in the first hour compared to colistin emphasize the potential as a fast-acting and potent antimicrobial against *P. aeruginosa*.

3.6. Synergy

Given the rapid bactericidal activity of TAT–ArgBD, we evaluated its ability to enhance the efficacy of existing antibiotics against PA14 bacteria. As a screening assay, the MIC reduction assay was conducted for several antibiotics, ceftazidime, chloramphenicol, colistimethate sodium (CMS), colistin, ciprofloxacin, imipenem, meropenem, and novobiocin, combined with just 0.5 μg/mL of TAT–ArgBD corresponding to a sublethal concentration (0.125-fold MIC). Synergistic effects were observed with 4 antibiotics, novobiocin, chloramphenicol, CMS, and imipenem, as shown in Fig. 11**a**. Since CMS is a prodrug and its active form, colistin, showed no promising synergy, both were excluded from follow-up studies. Subsequently, a follow-up bacterial inhibition checkerboard assay against *P. aeruginosa* PA14 was performed for the three synergistic antibiotics. As shown in Fig. 11**b**, TAT–ArgBD showed strong synergy with novobiocin, with a fractional inhibitory concentration index (FICI) of 0.25 and a maximum MIC reduction of 256-fold. Similar synergies were observed with imipenem, yielding a FICI of 0.375 and a maximum MIC reduction of 16-fold (Fig. 11**c**), while with chloramphenicol, resulting in a FICI of 0.312 and a maximum MIC reduction of 32-fold (Fig. 11**d**). It is particularly noteworthy, as summarized in Table 2, that antibiotics are typically active only against Gram-positive bacteria and inactive against *P. aeruginosa* synergized and became highly active against Gram-negative *P. aeruginosa.*

4. Discussion

Drug conjugation strategies, including antimicrobial peptide conjugation, have attracted attention as an efficient approach for enhancing their efficacy. RWK peptide conjugated to a methoxy core using a triazole linker improved the potency of the free RWK peptide against *A. baumannii* from > 100 μM to 7.5 μM (>13.3-fold)[57]. Glucose-cored glycocluster through a PEG and a triazole linkers(13aG/GalEG$_3$) could improve the antimicrobial efficacy for a multivalency of 4, compared to the monomeric form, which was improved 23–24 folds [58]. Complementary to such multivalent or scaffolded constructs, rationally engineered short AMPs built from coded and noncoded amino acids have recently demonstrated. These studies show that carefully tuned sequence amphipathicity can deliver nanomolar–micromolar activity, robust membrane permeabilization, and low hemolysis in vitro [59]. In this context, SR17, a short synthetic designer AMP, was shown to combine potent bacteriostatic and bactericidal activity against multiple strains. Its mechanism is linked to iron-transporting outer membrane proteins, reinforcing the concept that precisely engineered AMPs can exploit defined envelope components in Gram-negative pathogens [60]. Together, these studies highlight that both sequence-level design and supramolecular organization can be exploited to improve membrane-active antimicrobials.

TAT–ArgBD constitutes an amphiphilic, membrane-active modality, which has a length of 12–16 repeating units for optimal antimicrobial activity against both Gram-negative and Gram-positive bacteria—a criterion met by its material design [61]. On the other hand, this backbone-driven control of peptide conformation where aromatic amino (analogous to the carbazole moiety in ArgBD) acids are selected based on their conformational landscape to stabilize desired secondary structures in therapeutic peptides preferably after interacting with the target [62].

By conjugating the TAT peptide onto ArgBD with a multivalency of approximately 12, TAT–ArgBD achieved a more than 16-fold improvement compared to free TAT in terms of antimicrobial activity against *P. aeruginosa, S. aureus,* and *A. baumannii*. However, TAT conjugated to dextran showed no significant antimicrobial activity [14]. We speculate that the unique structure and characteristics of ArgBD enabled the TAT–ArgBD to interact with bacterial membranes due to the greater structural adaptability and significantly enhanced the potency of multivalent TAT. The flexible hexaethylene glycol spacer facilitates thermodynamically favorable structures of TAT, like an α-helix [63]. Additionally, ArgBD has previously been shown to interact selectively with the lipopolysaccharide (LPS) layer of Gram-negative bacteria and to induce local structural rearrangements at the lipid A interface. Embedding this LPS-binding scaffold into TAT–ArgBD is therefore expected to promote initial electrostatic docking and enrichment at Gram-negative cell surfaces, allowing TAT moieties to more efficiently engage and disorder the underlying anionic phospholipid bilayer. While direct visualization of LPS binding by TAT-ArgBD would provide more definitive evidence, the preserved ArgBD backbone makes it likely that this interaction is maintained and contributes to the overall membrane-disruptive and antibiotic-potentiating activity of the conjugate [22].

We compared the potency of TAT–ArgBD with colistin, an approved membrane-active antibiotic, as it represents the closest clinical analogue to the proposed mechanism of TAT-ArgBD. While colistin is an established antibiotic, its clinical use is limited due to renal toxicity and poor pharmacokinetics [64]. For example, a clinical study showed that colistin can cause acute kidney injury at concentrations as low as 2.2 μg/mL, which is above its breakpoint for *P. aeruginosa.* Hence, it is unlikely that colistin treats an infected patient without causing serious side effects [65]. However, predicting such effects with in vitro models beforehand is deemed very difficult due to many reasons including the inconsistency of the in vitro models reporting [66].

Although the proteolytic stability of TAT-ArgBD in plasma still needs to be established in additional studies, its single-digit-nanometer hydrodynamic diameter suggests it may evade rapid renal clearance and therefore achieve prolonged systemic exposure. Such prolonged exposure could be beneficial for PK/PD indices such as AUC/MIC. However, it may also represent a disadvantage. Long-circulating macromolecules and nanoparticles are often cleared slowly and may accumulate or be sequestered in organs such as the liver and spleen, particularly under repeated dosing, thereby increasing the risk of delayed or organ-specific toxicity. Therefore, the net benefit of prolonged exposure cannot be

Table 2
A summary of the MIC in PA14, the fold reduction in MIC of antibiotics synergized by TAT–ArgBD (2 μg/mL), and their known target-specific activities.

	MIC (μg/mL)		Fold MIC reduction	FICI	Activity against PA	Spectrum	Target
	w/o TAT–ArgBD	+ TAT–ArgBD					
Novobiocin	256	1	256	0.25	No	G+	DNA gyrase [54]
Imipenem	0.5	0.031	16	0.375	Yes (except CRPA)	Broad	Penicillin-binding proteins [55]
Chloramphenicol	32	1	32	0.312	No	Broad	70S ribosome [56]

inferred from the present in vitro dataset and will require dedicated *in vivo* pharmacokinetics, biodistribution/clearance, and single- and repeat-dose safety assessment [67–70]. Additionally, TAT-decorated nanostructures were observed to have a superior tissue penetration ability, so it has higher chances of reaching the site of infection [71]. Additionally, it is hinted in the literature that polymers with hydrophobic moieties might constitute a good option to penetrate biofilms and reach the targets within [72]. However, the PK/PD profile of TAT–ArgBD needs further investigation to confirm these expected advantages.

Conjugating peptides to the backbone to yield a multivalent construct often led to increased hemolysis of RBCs [12]. TAT–ArgBD showed a high 'membranolytic index,' defined here as the ratio of the hemolytic concentration to the antibacterial MIC (Hemolytic concertation/MIC), exceeding 64 under our assay conditions. This indicates a wide in vitro separation between antibacterial activity and erythrocyte lysis relative to amphiphilic cationic macromolecules [57,58,73,74]. This safety parameter becomes especially relevant in the case of IV systemic applications [75]. Interestingly, while isolated RBCs showed no lysis even above suspected therapeutic concentrations, mammalian cells were more susceptible to metabolic inhibition. For instance, 128 μg/mL (32-fold MIC) of TAT–ArgBD reduced metabolic activity (<15%), suggesting mitochondrial inhibition. At the same concentration, LDH cytotoxicity remained at 25–45%, indicating that cells were still partially intact. This phenomenon is hypothesized to be due to the TAT–ArgBD interactions with cardiolipin, which is a shared lipid between bacterial membranes and mitochondria [41,42]. In summary, TAT–ArgBD has an LDH CC_{50} (50% Cytotoxic Concentration) of $>$ 256 μg/mL, which yields a selectivity index (CC_{50}/MIC) of $>$ 64. To put this into perspective, colistin has an LDH CC_{50} of 25 μg/mL (50-fold MIC) with kidney cells, thus this highlights the potential for developing TAT–ArgBD further for *in vivo* experiments [76].

Beyond the safety profile, TAT–ArgBD demonstrates potent bactericidal activity. As per the Clinical and Laboratory Standards Institute (CLSI) guidelines, minimum bactericidal concentration (MBC) is defined as the 3-log decrease ($\geq$ 99.9%) of the inoculum in the time-kill assay [77]. This behavior is similar to other reported polymeric structures with positive surface charges, being able to kill different strains of bacteria with very high efficiency [78]. TAT–ArgBD could meet this criterion at a concentration of 32 μg/mL. Accordingly, the 1-hour MBC can be determined as 32 μg/mL. Notably, this concentration did not induce toxicity in all our safety studies, a key consideration for development for further development toward human use [79]. To put this into perspective, a study pooling 187 time-kill assays identified colistin as the most effective antibiotic in reducing persister survival among 54 antibiotics, while TAT–ArgBD outperformed colistin during the first hour [80]. At longer incubation times, this early superiority is diminished. This effect is likely attributable to the biodegradable nature of TAT–ArgBD and the protease susceptibility of its multivalent TAT moieties. Future explorative killing-kinetics studies could indeed unravel interesting bacterial killing patterns in other strains, especially with Gram-negative vs Gram-positive bacteria or with slowly growing Mycobacteria. In a closely related strategy, recently developed smart antimicrobial peptides (GDST-038, GDST-045 and their retro-inverso variants) achieve rapid killing of *A. baumannii* and *S. aureus* with minimal resistance development over 22 serial passages and low hemolysis, highlighting the potential of robust membrane-active agents to limit persister survival and resistance evolution [81].

Additionally, TAT–ArgBD exhibited potent activity against all tested strains except for *E. coli*. Based on our previous work, the ArgBD backbone preferentially accumulates and cluster at the bacterial surface rather than penetrate deeply into the cell envelope [22]. Accordingly, species-dependent susceptibility may not only depend on the overall anionic phospholipid content but also on how the respective cell envelope architectures (e.g., lateral lipid mobility) permitting such surface clustering of TAT–ArgBD. *E. coli* MG1655 strains possess rough, short LPS at the outer surface, whereas *P. aeruginosa* and *E. coli* ATCC 25922 produce smooth LPS. S. aureus does not express lipopolysaccharide at all. Such differences might influence the density and accessibility of anionic sites for productive cluster formation, although this was not directly investigated in our study and is technically very challenging to investigate. In this context, the comparatively higher MIC observed for *E. coli* MG1655 could be consistent with less favorable conditions for TAT–ArgBD clustering at the cell surface. At the same time, the lower activity against *E. coli* MG1655, which have rough LPS, raises the possibility of microbiome-sparing properties which merits further investigation [82–84].

In addition to the stand-alone antimicrobial activity, TAT–ArgBD could demonstrate strong potential as an adjuvant, converting Gram-positive or narrow-spectrum antibiotics into broad-spectrum antibiotics against *P. aeruginosa,* for instance. In a study by Krishnamoorthy et al., it was shown that *P. aeruginosa* with hyperporation could reduce the MIC of novobiocin, chloramphenicol, ciprofloxacin, and meropenem by 32-, 8-, 4-, and 4-fold, respectively [85]. Notably, this ranking of MIC reductions is the exact same as achieved by combining them with TAT–ArgBD. Together with the observations from SEM images (Fig. 4), the consistent reduction of MIC suggests pore formation as the mechanism of action of TAT–ArgBD. In addition, at higher concentrations, TAT–ArgBD can act as a stand-alone antibacterial agent using the same mechanism [86]. Because novobiocin has no EUCAST clinical breakpoints for human systemic infections, we used a published veterinary susceptibility target as a contextual reference. In bovine Mastitis isolates (staphylococci, streptococci, and Gram-negative isolates), an MIC of $\leq$ 4 μg/mL novobiocin was used to categorize isolates as susceptible; in our study, TAT–ArgBD reduced the novobiocin MIC in *P. aeruginosa* PA14–1 μg/mL, which is below this reported target and therefore encouraging, while requiring in vivo validation for clinical relevance [87,88]. In the case of chloramphenicol, the EUCAST susceptibility breakpoint is 2 μg/mL for most pathogens. Hence, 1 μg/mL of chloramphenicol, when combined with TAT–ArgBD, could be clinically actionable pending *in vivo* validation against *P. aeruginosa* infections [88]. Also, considering that imipenem activity against PA14 could be enhanced by TAT–ArgBD at concentrations as low as 0.031 μg/mL, such a low effective dose may be particularly relevant for carbapenem-resistant strains, but not as much to normally imipenem susceptible strains.

The pronounced MIC reductions observed for novobiocin, chloramphenicol, and imipenem are consistent with an envelope-driven potentiation mechanism, where antibiotic efficacy is primarily limited by restricted influx and/or active efflux in *P. aeruginosa*. Building on our prior findings for the ArgBD scaffold, we propose that the cationic TAT–ArgBD first enriches at the bacterial surface via electrostatic attraction and that the ArgBD backbone can locally loosen LPS packing through interactions at the lipid A region [22]. This surface "priming" would facilitate more effective, multivalent engagement of the outer membrane by the TAT moieties, promoting transient nanoscale defects and thereby increasing antibiotic access to downstream targets. Whether such defects propagate to the inner membrane cannot be concluded from the present data [89]. In this framework, novobiocin benefits from alleviated permeability constraints to reach its intracellular target (DNA gyrase), while chloramphenicol may additionally gain from increased intracellular accumulation if membrane perturbation transiently reduces efflux efficiency [90,91]. By contrast, imipenem acts on periplasmic PBPs, thus, even partial permeabilization of the outer membrane, granting enhanced periplasmic access, could explain the marked improvement in activity [92].

This mechanism of action was further explored by a variety of techniques, where pore-formation was shown with a non-lethal concentration of TAT–ArgBD. While these pores are probably caused by strong binding of TAT–ArgBD to POPG and cardiolipin, as shown by binding assays, leading to the formation of a more organized complex structure of TAT–ArgBD with the bacterial cell envelope, likely to be an

α-helical structure. The calcein-loaded vesicle leakage assay showed clear signs of TAT-ArgBD activity without the presence of LPS indicating that the conjugate is a versatile tool in against a number of bacterial strains. The trend observed in Fig. 8 starts in the range of 2–4 μg/mL, which also agrees with the MICs observed in Table 2. This similarity hints that intracellular components leakage via pore formation is the likely mechanism of action. Furthermore, SAXS suggests that the conjugate is partially embedded into the outer part of the vesicles. The combination of pore formation, local bilayer thinning, and increased area per lipid observed here is consistent with recent biophysical work on helical AMPs in bacterial lipid model membranes. These studies show that subtle thinning and softening of POPE/POPG or cardiolipin-containing bilayers correlate with high bactericidal activity, while similar effects in eukaryotic-like are associated with toxicity. Incorporating these insights, our data suggest that TAT–ArgBD achieves a similar biophysical signature of membrane destabilization, but in a way that remains largely confined to bacterial-type anionic lipid environments [93].

5. Conclusion

TAT–ArgBD is introduced as a novel multivalent antimicrobial conjugate which addresses critical gaps in combating bacterial infections. The resulting construct demonstrated potent antibacterial activity against both Gram-negative (*P. aeruginosa* and *A. baumannii*) as well as Gram-positive (*S. aureus*) bacteria, by improving the activity of free TAT by tens of folds (MICs as low as 2 μg/mL) and a rapid onset of action (1-hour MBC of 32 μg/mL). Additionally, TAT–ArgBD showed synergy with antibiotics like novobiocin, chloramphenicol, and imipenem, enhancing their efficacy against Gram-negative bacteria and expanding (in the case of novobiocin) the spectrum of activity from Gram-positive to encompass Gram-negative pathogens. Mechanistic studies showed that TAT–ArgBD operates through bacterial membrane pore formation and orders the structure of TAT–ArgBD to an α-helical structure by embedding into POPG and cardiolipin lipids of the bacterial cell envelope.

Besides the potential use of TAT–ArgBD as a single-agent anti-infective and as a synergistically acting agent in combination therapy, its lower antibacterial activity against *E. coli* compared to exclusively pathogenic bacteria also suggests putatively microbiome-sparing properties. Our results suggest that dynamically bio-responsive polymers, like biodynamers, functionalized with multiple membrane-active peptides, enable unique molecular interactions with bacterial membranes in addition to the intrinsic ability of ArgBD to interact with the LPS layer [22]. This may distinguish them from other polymeric constructs, such as dendrimers, PLGA-, or dextran-based backbones. Biodynamer constructs may provide a promising route to develop highly potent and safe antibacterial therapeutics, especially against MDR infections by some clinically relevant pathogens. The promising *in vitro* profile serves as a starting point for future *in vivo* validation. An important next step will be to validate TAT–ArgBD and related constructs on MDR clinical isolates, in particular strains in which reduced permeability (porin loss or LPS modifications) to confirm that the antibiotic-potentiating effect observed here translates to clinically relevant settings. Accordingly, future studies that adapt and optimize this platform for other peptides, as well as explore its utility for local or systemic applications in complex *in vitro* models or *in vivo* using resistant strains, could establish this system as a strategy to overcome the limitations of conventional antibiotics.

CRediT authorship contribution statement

Hirsch Anna K. H.: Writing – review & editing, Supervision, Resources, Conceptualization. **Marcus Koch:** Validation, Resources, Methodology, Investigation. **Jennifer Herrmann:** Validation, Resources, Methodology, Investigation. **Justine Bassil:** Writing – original draft, Validation, Methodology. **Walaa M. Metwally:** Writing – review & editing, Methodology, Investigation. **Tobias Kraus:** Supervision, Resources, Methodology. **Bart-Jan Niebuur:** Visualization, Validation, Software, Methodology, Investigation, Formal analysis, Data curation. **Sangeun Lee:** Writing – review & editing, Writing – original draft, Visualization, Supervision, Project administration, Conceptualization. **Brigitta Loretz:** Writing – review & editing, Writing – original draft, Visualization, Supervision, Project administration, Funding acquisition, Conceptualization. **Kamal Mohamed A. M.:** Writing – review & editing, Writing – original draft, Validation, Software, Methodology, Investigation, Formal analysis, Data curation, Conceptualization. **Claus-Michael Lehr:** Writing – review & editing, Writing – original draft, Supervision, Resources, Project administration, Funding acquisition, Conceptualization.

Declaration of Competing Interest

The authors declare that they have no known competing financial interests or personal relationships that could have appeared to influence the work reported in this paper.

Acknowledgement

The authors would like to thank, Pascal Paul for help with SEM imaging, Petra König for help with cell culture, Dr. Sari Rasheed, Dr. Annette Boese, Alexandra Amann, Viktoria George for help with antimicrobial assays. Dr. Jia-Jhen Kang (NSRRC) is acknowledged for valuable discussions on the interpretation of the SAXS data.

Walaa M. Metwally is funded by the European Union (TALENTS Project, Grant Agreement Number 101081463). Views and opinions expressed are however those of the author(s) only and do not necessarily reflect those of the European Union. Neither the European Union nor the granting authority can be held responsible for them.

Appendix A. Supporting information

Supplementary data associated with this article can be found in the online version at doi:10.1016/j.biopha.2026.119304.

Data availability

Data will be made available on request.

References

[1] WHO, WHO bacterial priority pathogens list, 2024, bacterial pathogens of public health importance to guide research, Dev. Strateg. Prev. Control Antimicrob. Resist. 72 (2024). ⟨https://www.who.int/publications/i/item/9789240093461⟩.

[2] E. Tacconelli, E. Carrara, A. Savoldi, S. Harbarth, M. Mendelson, D.L. Monnet, C. Pulcini, G. Kahlmeter, J. Kluytmans, Y. Carmeli, M. Ouellette, K. Outterson, J. Patel, M. Cavaleri, E.M. Cox, C.R. Houchens, M.L. Grayson, P. Hansen, N. Singh, U. Theuretzbacher, N. Magrini, A.O. Aboderin, S.S. Al-Abri, N. Awang Jalil, N. Benzonana, S. Bhattacharya, A.J. Brink, F.R. Burkert, O. Cars, G. Cornaglia, O. J. Dyar, A.W. Friedrich, A.C. Gales, S. Gandra, C.G. Giske, D.A. Goff, H. Goossens, T. Gottlieb, M. Guzman Blanco, W. Hryniewicz, D. Kattula, T. Jinks, S.S. Kanj, L. Kerr, M.P. Kieny, Y.S. Kim, R.S. Kozlov, J. Labarca, R. Laxminarayan, K. Leder, L. Leibovici, G. Levy-Hara, J. Littman, S. Malhotra-Kumar, V. Manchanda, L. Moja, B. Ndoye, A. Pan, D.L. Paterson, M. Paul, H. Qiu, P. Ramon-Pardo, J. Rodríguez-Baño, M. Sanguinetti, S. Sengupta, M. Sharland, M. Si-Mehand, L.L. Silver, W. Song, M. Steinbakk, J. Thomsen, G.E. Thwaites, J.W. van der Meer, N. Van Kinh, S. Vega, M.V. Villegas, A. Wechsler-Fördös, H.F.L. Wertheim, E. Wesangula, N. Woodford, F.O. Yilmaz, A. Zorzet, Discovery, research, and development of new antibiotics: the WHO priority list of antibiotic-resistant bacteria and tuberculosis, Lancet Infect. Dis. 18 (2018) 318–327, https://doi.org/10.1016/S1473-3099(17)30753-3.

[3] A. Bali, M.A.M. Kamal, G. Mulla, B. Loretz, C.M. Lehr, Functional materials to overcome bacterial barriers and models to advance their development, Adv. Funct. Mater. 33 (2023) 2304370, https://doi.org/10.1002/adfm.202304370.

[4] R.F. Langendonk, D.R. Neill, J.L. Fothergill, The building blocks of antimicrobial resistance in pseudomonas aeruginosa: implications for current resistance-breaking therapies, Front Cell Infect. Microbiol. 11 (2021) 665759, https://doi.org/10.3389/FCIMB.2021.665759.

[5] M.E. Falagas, S.K. Kasiakou, Toxicity of polymyxins: a systematic review of the evidence from old and recent studies, Crit. Care 10 (2006) R27, https://doi.org/10.1186/CC3995.

[6] M. Borowiak, J. Fischer, J.A. Hammerl, R.S. Hendriksen, I. Szabo, B. Malorny, Identification of a novel transposon-associated phosphoethanolamine transferase gene, mcr-5, conferring colistin resistance in d-tartrate fermenting Salmonella enterica subsp. enterica serovar Paratyphi B, J. Antimicrob. Chemother. 72 (2017) 3317–3324, https://doi.org/10.1093/JAC/DKX327.

[7] E. Kim, J. Yang, S. Park, K. Shin, Factors affecting success of new drug clinical trials, Ther. Innov. Regul. Sci. 57 (2023) 737–750, https://doi.org/10.1007/S43441-023-00509-1.

[8] Antibacterial products in clinical development for priority pathogens, (n.d.). ⟨https://www.who.int/observatories/global-observatory-on-health-research-and-development/monitoring/antibacterial-products-in-clinical-development-for-priority-pathogens⟩ (accessed December 1, 2024).

[9] H.D. Herce, A.E. Garcia, Molecular dynamics simulations suggest a mechanism for translocation of the HIV-1 TAT peptide across lipid membranes, Proc. Natl. Acad. Sci. USA 104 (2007) 20805–20810, https://doi.org/10.1073/PNAS.0706574105.

[10] F. Her Choong, B. Keat Yap, Cell-penetrating peptides: correlation between peptide-lipid interaction and penetration efficiency, ChemPhysChem. 22 (2021) 493–498, https://doi.org/10.1002/CPHC.202000873.

[11] J. Reeman, L.M. Ittner, K.A. Vallis, O. Tietz, Strength in numbers: cell penetrating peptide clusters to build next-generation therapeutics, Trends Chem. 6 (2024) 669–683, https://doi.org/10.1016/J.TRECHM.2024.09.003/ASSET/56B0B991-1212-4D0E-97D7-93C0C4512123/MAIN.ASSETS/GR4.JPG.

[12] S.P. Liu, L. Zhou, R. Lakshminarayanan, R.W. Beuerman, Multivalent antimicrobial peptides as therapeutics: design principles and structural diversities, Int. J. Pept. Res. Ther. 16 (2010) 199–213, https://doi.org/10.1007/S10989-010-9230-Z.

[13] J.P. Tam, Y.A. Lu, J.L. Yang, Antimicrobial dendrimeric peptides, Eur. J. Biochem. 269 (2002) 923–932, https://doi.org/10.1046/J.0014-2956.2001.02728.X.

[14] L.W. Chan, K.E. Hern, C. Ngambenjawong, K. Lee, E.J. Kwon, D.T. Hung, S. N. Bhatia, Selective permeabilization of gram-negative bacterial membranes using multivalent peptide constructs for antibiotic sensitization, ACS Infect. Dis. 7 (2021) 721–732, https://doi.org/10.1021/acsinfecdis.0c00805.

[15] Y. Lin, Y. Zhang, X. Cai, H. He, C. Yang, J. Ban, B. Guo, Design and self-assembly of peptide-copolymer conjugates into nanoparticle hydrogel for wound healing in diabetes, Int J. Nanomed. 19 (2024) 2487–2506, https://doi.org/10.2147/IJN.S452915.

[16] S. Li, S. Qiang, J. Wang, T. Yang, L. Jiang, Y. Zhang, Y. Chen, Structure, stability, and mechanism of dextran–CPP–Ca2+ conjugates: a novel high-efficiency calcium ion delivery system, Food Chem. 408 (2023) 135190, https://doi.org/10.1016/J.FOODCHEM.2022.135190.

[17] B. Lebleu, H.M. Moulton, R. Abes, G.D. Ivanova, S. Abes, D.A. Stein, P.L. Iversen, A. A. Arzumanov, M.J. Gait, Cell penetrating peptide conjugates of steric block oligonucleotides, Adv. Drug Deliv. Rev. 60 (2008) 517–529, https://doi.org/10.1016/J.ADDR.2007.09.002.

[18] S. Lee, S. Nasr, S. Rasheed, Y. Liu, O. Hartwig, C. Kaya, A. Boese, M. Koch, J. Herrmann, R. Müller, B. Loretz, E. Buhler, A.K.H.H. Hirsch, C.-M.M. Lehr, A. K. H, C.-M.M. Lehr, A.K.H.H. Hirsch, A.K.H. Hirsch, Proteoid biodynamers for safe mRNA transfection via pH-responsive nanorods enabling 1 endosomal escape Introductory paragraph 20, J. Control. Release 353 (2023) 915–929, https://doi.org/10.1016/J.JCONREL.2022.12.018.

[19] Y. Liu, J.M. Lehn, A.K.H. Hirsch, Molecular biodynamers: dynamic covalent analogues of biopolymers, Acc. Chem. Res 50 (2017) 376–386, https://doi.org/10.1021/acs.accounts.6b00594.

[20] S. Lee, C. Kaya, H. Jang, M. Koch, B. Loretz, E. Buhler, C.M. Lehr, A.K.H. Hirsch, PH-Dependent morphology and optical properties of lysine-derived molecular biodynamers, Mater. Chem. Front 4 (2020) 905–909, https://doi.org/10.1039/c9qm00651f.

[21] Y. Liu, M.C.A. Stuart, E. Buhler, J.M. Lehn, A.K.H. Hirsch, Proteoid dynamers with tunable properties, Adv. Funct. Mater. 26 (2016) 6297–6305, https://doi.org/10.1002/ADFM.201601612.

[22] M.A.M. Kamal, J. Bassil, B. Loretz, A.K.H. Hirsch, S. Lee, C.M. Lehr, Arg-biodynamers as antibiotic potentiators through interacting with Gram-negative outer membrane lipopolysaccharides, Eur. J. Pharm. Biopharm. 200 (2024) 114336, https://doi.org/10.1016/J.EJPB.2024.114336.

[23] G.F. Pauli, T. Gödecke, B.U. Jaki, D.C. Lankin, Quantitative ^{1}H NMR. development and potential of an analytical method: an update, J. Nat. Prod. 75 (2012) 834–851, https://doi.org/10.1021/NP200993K.

[24] A. Yammine, J. Gao, A.H. Kwan, Tryptophan fluorescence quenching assays for measuring protein-ligand binding affinities: principles and a practical guide, Bio. Protoc. 9 (2019), https://doi.org/10.21769/BIOPROTOC.3253.

[25] P.J. Wyatt, Light scattering and the absolute characterization of macromolecules, Anal. Chim. Acta 272 (1993) 1–40, https://doi.org/10.1016/0003-2670(93)80373-S.

[26] J. Stetefeld, S.A. McKenna, T.R. Patel, Dynamic light scattering: a practical guide and applications in biomedical sciences, Biophys. Rev. 4 8 (2016) 409–427, https://doi.org/10.1007/S12551-016-0218-6.

[27] A. Savitzky, M.J.E. Golay, Smoothing and differentiation of data by simplified least squares procedures, Anal. Chem. 36 (2002) 1627–1639, https://doi.org/10.1021/AC60214A047.

[28] S.R. Dennison, D.A. Phoenix, Susceptibility of sheep, human, and pig erythrocytes to haemolysis by the antimicrobial peptide Modelin 5, Eur. Biophys. J. 43 (2014) 423–432, https://doi.org/10.1007/S00249-014-0974-9.

[29] J.F. Kreisberg, N.T. Ong, A. Krishna, T.L. Joseph, J. Wang, C. Ong, H.A. Ooi, J. C. Sung, C.C. Siew, G.C. Chang, F. Biot, J. Cuccui, B.W. Wren, J. Chan, S. P. Sivalingam, L.H. Zhang, C. Verma, P. Tan, Growth inhibition of pathogenic bacteria by sulfonylurea herbicides, Antimicrob. Agents Chemother. 57 (2013) 1513–1517, https://doi.org/10.1128/AAC.02327-12.

[30] J.M. Schuurmans, A.S. Nuri Hayali, B.B. Koenders, B.H. ter Kuile, Variations in MIC value caused by differences in experimental protocol, J. Microbiol. Methods 79 (2009) 44–47, https://doi.org/10.1016/J.MIMET.2009.07.017.

[31] S. Štumpf, G. Hostnik, M. Primožič, M. Leitgeb, J.P. Salminen, U. Bren, The Effect of Growth Medium Strength on Minimum Inhibitory Concentrations of Tannins and Tannin Extracts against E. coli, Molecules 25 (2020) 2947, https://doi.org/10.3390/MOLECULES25122947.

[32] D. Hörömpöli, C. Ciglia, K.H. Glüsenkamp, L.O. Haustedt, H. Falkenstein-Paul, G. Bendas, A. Berscheid, H. Brötz-Oesterhelt, The antibiotic negamycin crosses the bacterial cytoplasmic membrane by multiple routes, Antimicrob. Agents Chemother. 65 (2021), https://doi.org/10.1128/AAC.00986-20.

[33] D.K. Mercer, M.D.T. Torres, S.S. Duay, E. Lovie, L. Simpson, M. von Köckritz-Blickwede, C. de la Fuente-Nunez, D.A. O'Neil, A.M. Angeles-Boza, Antimicrobial susceptibility testing of antimicrobial peptides to better predict efficacy, Front Cell Infect. Microbiol. 10 (2020) 540826, https://doi.org/10.3389/FCIMB.2020.00326/BIBTEX.

[34] N. Fatsis-Kavalopoulos, D.L. Sánchez-Hevia, D.I. Andersson, Beyond the FIC index: the extended information from fractional inhibitory concentrations (FICs), J. Antimicrob. Chemother. 79 (2024) 2394, https://doi.org/10.1093/JAC/DKAE233.

[35] S. Subramaniam, P. Joyce, C.E. Conn, C.A. Prestidge, Cellular uptake and in vitro antibacterial activity of lipid-based nanoantibiotics are influenced by protein corona, Biomater. Sci. 12 (2024) 3411–3422, https://doi.org/10.1039/D4BM00608A.

[36] N. Bankar, L. Latta, B. Loretz, B. Reda, J. Dudek, H. Hähl, M. Hannig, C.M. Lehr, Antimicrobial and antibiotic-potentiating effect of calcium peroxide nanoparticles on oral bacterial biofilms, Npj Biofilms Micro 10 (2024) 106, https://doi.org/10.1038/s41522-024-00569-7.

[37] J. Dubochet, M. Adrian, J. Lepault, A.W. McDowall, Emerging techniques: Cryo-electron microscopy of vitrified biological specimens, Trends Biochem. Sci. 10 (1985) 143–146, https://doi.org/10.1016/0968-0004(85)90150-1.

[38] B. Hammouda, Analysis of the Beaucage model, Urn:Issn:0021-8898 43 (2010) 1474–1478. https://doi.org/10.1107/S0021889810033856.

[39] T. Ben-Nun, A. Ginsburg, P. Székely, U. Raviv, X+: a comprehensive computationally accelerated structure analysis tool for solution X-ray scattering from supramolecular self-assemblies, J. Appl. Crystallogr 43 (2010) 1522–1531, https://doi.org/10.1107/S0021889810032772/AJ5158SUP2.PDF.

[40] B.M. Tande, N.J. Wagner, M.E. Mackay, C.J. Hawker, M. Jeong, Viscosimetric, hydrodynamic, and conformational properties of dendrimers and dendrons, Macromolecules 34 (2001) 8580–8585, https://doi.org/10.1021/MA011265G/ASSET/MA011265G.FP.PNG_V03.

[41] S.E. Horvath, G. Daum, Lipids of mitochondria, Prog. Lipid Res. 52 (2013) 590–614, https://doi.org/10.1016/J.PLIPRES.2013.07.002.

[42] K. Boguszewska, M. Szewczuk, J. Kazmierczak-Baranska, B.T. Karwowski, The similarities between human mitochondria and bacteria in the context of structure, genome, and base excision repair system, Molecules 25 (2020) 2857, https://doi.org/10.3390/MOLECULES25122857.

[43] Y. Rao, S.J.J. Kwok, J. Lombardi, N.J. Turro, K.B. Eisenthal, Label-free probe of HIV-1 TAT peptide binding to mimetic membranes, Proc. Natl. Acad. Sci. USA 111 (2014) 12684–12688, https://doi.org/10.1073/PNAS.1411817111.

[44] H. Nikaido, Molecular basis of bacterial outer membrane permeability revisited, Microbiol. Mol. Biol. Rev. 67 (2003) 593–656, https://doi.org/10.1128/mmbr.67.4.593-656.2003.

[45] H. Nikaido, M. Vaara, Molecular basis of bacterial outer membrane permeability, Microbiol. Rev. 49 (1985) 1–32, https://doi.org/10.1128/mmbr.49.1.1-32.1985.

[46] K. Zhang, H. Zhang, C. Gao, R. Chen, C. Li, Antimicrobial Mechanism of pBD2 against Staphylococcus aureus, Molecules 25 (2020) 3513, https://doi.org/10.3390/MOLECULES25153513.

[47] M. Hartmann, M. Berditsch, J. Hawecker, M.F. Ardakani, D. Gerthsen, A.S. Ulrich, Damage of the bacterial cell envelope by antimicrobial peptides gramicidin S and PGLa as revealed by transmission and scanning electron microscopy, Antimicrob. Agents Chemother. 54 (2010) 3132–3142, https://doi.org/10.1128/AAC.00124-10;CTYPE:STRING:JOURNAL.

[48] T.W. Hsu, C.H. Yang, C.J. Su, Y.T. Huang, Y.Q. Yeh, K.F. Liao, T.C. Lin, O. Shih, M. T. Lee, A.C. Su, U.S. Jeng, J. Trewhella, Revealing cholesterol effects on PEGylated HSPC liposomes using AF4-MALS and simultaneous small- and wide-angle X-ray scattering, J. Appl. Crystallogr 56 (2023) 988–993, https://doi.org/10.1107/S1600576723005393/TJ5034SUP1.PDF.

[49] E. Krok, M. Stephan, R. Dimova, L. Piatkowski, Tunable biomimetic bacterial membranes from binary and ternary lipid mixtures and their application in antimicrobial testing, Biochim. Et. Biophys. Acta (BBA) Biomembr. 1865 (2023) 184194, https://doi.org/10.1016/J.BBAMEM.2023.184194.

[50] S. Dutta, B.G. Watson, S. Mattoo, J.C. Rochet, Calcein release assay to measure membrane permeabilization by recombinant alpha-synuclein, Bio Protoc. 10 (2020), https://doi.org/10.21769/BIOPROTOC.3690.

[51] R. Usha, T. Ramasami, The effects of urea and n-propanol on collagen denaturation: using DSC, circular dicroism and viscosity, Thermochim. Acta 409 (2004) 201–206, https://doi.org/10.1016/S0040-6031(03)00335-6.
[52] S.M. Kelly, N.C. Price, Circular dichroism: studies of proteins, Encycl. Life Sci. (2009), https://doi.org/10.1002/9780470015902.A0003043.PUB2.
[53] A. Kefala, M. Amprazi, E. Mylonas, D. Kotsifaki, M. Providaki, C. Pozidis, M. Fotiadou, M. Kokkinidis, Probing protein folding with sequence-reversed α-helical bundles, Int. J. Mol. Sci. 22 (2021) 1955, https://doi.org/10.3390/IJMS22041955.
[54] M.D. Mandler, V. Baidin, J. Lee, K.S. Pahil, T.W. Owens, D. Kahne, Novobiocin enhances polymyxin activity by stimulating lipopolysaccharide transport, J. Am. Chem. Soc. 140 (2018) 6749–6753, https://doi.org/10.1021/JACS.8B02283.
[55] Y. Yang, N. Bhachech, K. Bush, Biochemical comparison of imipenem, meropenem and biapenem: permeability, binding to penicillin-binding proteins, and stability to hydrolysis by β-lactamases, J. Antimicrob. Chemother. 35 (1995) 75–84, https://doi.org/10.1093/JAC/35.1.75.
[56] M.S. Svetlov, E. Plessa, C.W. Chen, A. Bougas, M.G. Krokidis, G.P. Dinos, Y. S. Polikanov, High-resolution crystal structures of ribosome-bound chloramphenicol and erythromycin provide the ultimate basis for their competition, RNA 25 (2019) 600–606, https://doi.org/10.1261/RNA.069260.118.
[57] B.C. Hoffknecht, D.J. Worm, S. Bobersky, P. Prochnow, J.E. Bandow, N. Metzler-Nolte, Influence of the multivalency of ultrashort arg-trp-based antimicrobial peptides (AMP) on their antibacterial activity, ChemMedChem 10 (2015) 1564–1569, https://doi.org/10.1002/CMDC.201500220.
[58] S. Cecioni, J.P. Praly, S.E. Matthews, M. Wimmerová, A. Imberty, S. Vidal, Rational design and synthesis of optimized glycoclusters for multivalent lectin–carbohydrate interactions: influence of the linker arm, Chem. A Eur. J. 18 (2012) 6250–6263, https://doi.org/10.1002/CHEM.201200010.
[59] L.M. Behera, M. Ghosh, P.K. Gupta, S. Rana, A rationally engineered small antimicrobial peptide with potent antibacterial activity, J. Cell Biochem. 125 (2024) e30503, https://doi.org/10.1002/JCB.30503;REQUESTEDJOURNAL:JOURNAL:10974644;JOURNAL:JOURNAL:15479366;WGROUP:STRING:PUBLICATION.
[60] S. Shadangi, A. Singh, S. Rana, Deciphering the mechanism of action of a short, synthetic designer amp against gram-negative bacteria, Biopolymers 116 (2025) e70019, https://doi.org/10.1002/BIP.70019;PAGE:STRING:ARTICLE/CHAPTER.
[61] J. Klousnitzer, W. Xiang, V.M. Polynice, B. Deslouches, Comparative properties of helical and linear amphipathicity of peptides composed of arginine, tryptophan, and valine, Antibiotics 13 (2024) 954, https://doi.org/10.3390/ANTIBIOTICS13100954/S1.
[62] L.M. Behera, M. Ghosh, S. Rana, Deciphering the conformational landscape of few selected aromatic noncoded amino acids (NCAAs) for applications in rational design of peptide therapeutics, Amino Acids 54 (2022) 1183–1202, https://doi.org/10.1007/S00726-022-03175-Z.
[63] A.K.H.H. Hirsch, E. Buhler, J.M. Lehn, Biodynamers: self-organization-driven formation of doubly dynamic proteoids, J. Am. Chem. Soc. 134 (2012) 4177–4183, https://doi.org/10.1021/ja2099134.
[64] R.L. Nation, J. Li, Colistin in the 21st century, Curr. Opin. Infect. Dis. 22 (2009) 535–543, https://doi.org/10.1097/QCO.0B013E328332E672.
[65] L. Sorlí, S. Luque, S. Grau, N. Berenguer, C. Segura, M.M. Montero, F. Álvarez-Lerma, H. Knobel, N. Benito, J.P. Horcajada, Trough colistin plasma level is an independent risk factor for nephrotoxicity: a prospective observational cohort study, BMC Infect. Dis. 13 (2013) 1–9, https://doi.org/10.1186/1471-2334-13-380.
[66] S. Subramaniam, P. Joyce, A.D. Ogunniyi, A. Dube, S.L. Sampson, C.M. Lehr, C. A. Prestidge, Minimum information for conducting and reporting in vitro intracellular infection assays, ACS Infect. Dis. 10 (2024) 337–349, https://doi.org/10.1021/ACSINFECDIS.3C00613/ASSET/IMAGES/MEDIUM/ID3C00613_0004.GIF.
[67] M.P. Bohrer, C. Baylis, H.D. Humes, R.J. Glassock, C.R. Robertson, B.M. Brenner, Permselectivity of the glomerular capillary wall: facilitated filtration of circulating polycations, J. Clin. Invest 61 (1978) 72–78, https://doi.org/10.1172/JCI108927.
[68] S.N. Tammam, H.M.E. Azzazy, A. Lamprecht, Biodegradable particulate carrier formulation and tuning for targeted drug delivery, J. Biomed. Nanotechnol. 11 (2015) 555–577, https://doi.org/10.1166/JBN.2015.2017.
[69] A.C. Anselmo, V. Gupta, B.J. Zern, D. Pan, M. Zakrewsky, V. Muzykantov, S. Mitragotri, Delivering nanoparticles to lungs while avoiding liver and spleen through adsorption on red blood cells, ACS Nano 7 (2013) 11129–11137, https://doi.org/10.1021/NN404853Z.
[70] B. Du, X. Jiang, A. Das, Q. Zhou, M. Yu, R. Jin, J. Zheng, Glomerular barrier behaves as an atomically precise bandpass filter in a sub-nanometre regime, Nat. Nanotechnol. 12 (2017) 1096–1102, https://doi.org/10.1038/nnano.2017.170.
[71] Z. Li, W. Pan, E. Shi, L. Bai, H. Liu, C. Li, Y. Wang, J. Deng, Y. Wang, A multifunctional nanosystem based on bacterial cell-penetrating photosensitizer for fighting periodontitis via combining photodynamic and antibiotic therapies, ACS Biomater. Sci. Eng. (2021), https://doi.org/10.1021/acsbiomaterials.0c01638.
[72] F. Soukarieh, P. Gurnani, M. Romero, N. Halliday, M. Stocks, C. Alexander, M. Cámara, Design of quorum sensing inhibitor-polymer conjugates to penetrate pseudomonas aeruginosa biofilms, ACS Macro. Lett. 12 (2023) 314–319, https://doi.org/10.1021/ACSMACROLETT.2C00699/ASSET/IMAGES/LARGE/MZ2C00699_0004.JPEG.
[73] B.C. Hoffknecht, H.B. Albada, M. Sturm, P. Prochnow, J.E. Bandow, N. Metzler-Nolte, Synthesis and antibacterial activity of trivalent ultrashort Arg-Trp-based antimicrobial peptides (AMPs), Medchemcomm. 6 (2015) 372–376, https://doi.org/10.1039/c4md00327f.
[74] M.M. Konai, B. Bhattacharjee, S. Ghosh, J. Haldar, Recent progress in polymer research to tackle infections and antimicrobial resistance, Biomacromolecules 19 (2018) 1888–1917, https://doi.org/10.1021/ACS.BIOMAC.8B00458.
[75] N. Ilić, M. Novković, F. Guida, D. Xhindoli, M. Benincasa, A. Tossi, D. Juretić, Selective antimicrobial activity and mode of action of adepantins, glycine-rich peptide antibiotics based on anuran antimicrobial peptide sequences, Biochim. Et. Biophys. Acta (BBA) Biomembr. 1828 (2013) 1004–1012, https://doi.org/10.1016/J.BBAMEM.2012.11.017.
[76] A. Gallardo-Godoy, C. Muldoon, B. Becker, A.G. Elliott, L.H. Lash, J.X. Huang, M. S. Butler, R. Pelingon, A.M. Kavanagh, S. Ramu, W. Phetsang, M.A.T. Blaskovich, M.A. Cooper, Activity and predicted nephrotoxicity of synthetic antibiotics based on polymyxin B, J. Med Chem. 59 (2016) 1068–1077, https://doi.org/10.1021/ACS.JMEDCHEM.5B01593/SUPPL_FILE/JM5B01593_SI_002.CSV.
[77] M26 AE Bactericidal Activity of Antimicrobial Agents, (n.d.).(accessed August 18, 2024)⟨https://clsi.org/standards/products/microbiology/documents/m26/⟩.
[78] J. Park, Z. Xiang, Y. Liu, C.H. Li, C. Chen, H. Nagaraj, T. Nguyen, A. Nabawy, H. Koo, V.M. Rotello, Surface-charge tuned polymeric nanoemulsions for carvacrol delivery in interkingdom biofilms, ACS Appl. Mater. Interfaces 16 (2024) 37613–37622, https://doi.org/10.1021/ACSAMI.4C06618/SUPPL_FILE/AM4C06618_SI_001.PDF.
[79] W. Couet, N. Grégoire, P. Gobin, P.J. Saulnier, D. Frasca, S. Marchand, O. Mimoz, Pharmacokinetics of colistin and colistimethate sodium after a single 80-mg intravenous dose of CMS in young healthy volunteers, Clin. Pharm. Ther. 89 (2011) 875–879, https://doi.org/10.1038/CLPT.2011.48.
[80] J.E. Salcedo-Sora, D.B. Kell, A quantitative survey of bacterial persistence in the presence of antibiotics: towards antipersister antimicrobial discovery, Antibiotics 9 (2020) 508, https://doi.org/10.3390/ANTIBIOTICS9080508.
[81] D. Schillaci, G. Babuççu, N. Vavilthota, C. Bournez, L. de Boer, R.A. Cordfunke, P. H. Nibbering, G.J.P. van Westen, J.W. Drijfhout, S.A.J. Zaat, M. Riool, Machine learning-identified potent antimicrobial peptides against multidrug-resistant bacteria and skin infections, Antibiotics 14 (2025) 1172, https://doi.org/10.3390/ANTIBIOTICS14111172.
[82] G. Reid, J. Howard, B.S. Gan, Can bacterial interference prevent infection? Trends Microbiol. 9 (2001) 424–428, https://doi.org/10.1016/S0966-842X(01)02132-1.
[83] S.M. Huszczynski, J.S. Lam, C.M. Khursigara, The role of pseudomonas aeruginosa lipopolysaccharide in bacterial pathogenesis and physiology, Pathogens 9 (2019) 6, https://doi.org/10.3390/PATHOGENS9010006.
[84] D. Liu, P.R. Reeves, Escherichia coli K12 regains its O antigen, Microbiol. 140 (1994) 49–57, https://doi.org/10.1099/13500872-140-1-49/CITE/REFWORKS.
[85] G. Krishnamoorthy, I.V. Leus, J.W. Weeks, D. Wollosheck, V.V. Rybenkov, H. I. Zgurskaya, Synergy between active efflux and outer membrane diffusion defines rules of antibiotic permeation into gram-negative bacteria, MBio 8 (2017), https://doi.org/10.1128/MBIO.01172-17.
[86] X. Zhang, Z. Zhang, Q. Shu, C. Xu, Q. Zheng, Z. Guo, C. Wang, Z. Hao, X. Liu, G. Wang, W. Yan, H. Chen, C. Lu, Copper clusters: an effective antibacterial for eradicating multidrug-resistant bacterial infection in vitro and in vivo, Adv. Funct. Mater. 31 (2021) 2008720, https://doi.org/10.1002/ADFM.202008720.
[87] eucast: Clinical breakpoints and dosing of antibiotics, (n.d.). ⟨https://www.eucast.org/clinical_breakpoints⟩ (accessed October 8, 2024).
[88] C. Thornsberry, P.J. Burton, Y.C. Yee, J.L. Watts, R.J. Yancey, The activity of a combination of penicillin and novobiocin against bovine mastitis pathogens: development of a disk diffusion test, J. Dairy Sci. 80 (1997) 413, https://doi.org/10.3168/jds.S0022-0302(97)75952-6.
[89] G. Krishnamoorthy, I.V. Leus, J.W. Weeks, D. Wollosheck, V.V. Rybenkov, H. I. Zgurskaya, Synergy between active efflux and outer membrane diffusion defines rules of antibiotic permeation into Gram-negative bacteria, MBio 8 (2017) 1–16, https://doi.org/10.1128/mBio.01172-17.
[90] Y. Morita, J. Tomida, Y. Kawamura, MexXY multidrug efflux system of pseudomonas aeruginosa, Front Microbiol. 3 (2012) 38395, https://doi.org/10.3389/FMICB.2012.00408.
[91] F. Collin, S. Karkare, A. Maxwell, Exploiting bacterial DNA gyrase as a drug target: current state and perspectives, Appl. Microbiol. Biotechnol. 92 (2011) 479–497, https://doi.org/10.1007/S00253-011-3557-Z.
[92] S. Nepal, S. MaaB, S. Grasso, F.M. Cavallo, J. Bartel, D. Becher, E. Bathoorn, J. M. Van Dijl, Proteomic charting of imipenem adaptive responses in a highly carbapenem resistant clinical Enterobacter roggenkampii isolate, Antibiotics 10 (2021) 501, https://doi.org/10.3390/ANTIBIOTICS10050501/S1.
[93] S. Mitra, M.T. Chen, F. Stedman, J. Hernandez, G. Kumble, X. Kang, C. Zhang, G. Tang, I. Daugherty, W. Liu, J. Ocloo, K.R. Klucznik, A.A. Li, F. Heinrich, B. Deslouches, S. Tristram-Nagle, How unnatural amino acids in antimicrobial peptides change interactions with lipid model membranes, J. Phys. Chem. B 128 (2024) 9772–9784, https://doi.org/10.1021/ACS.JPCB.4C04152.